AGU PUBLICATIONS

Geochemistry, Geophysics, Geosystems

RESEARCH ARTICLE
10.1002/2013GC005069

Key Points:
- Analysis of high-resolution 3-D MCS data resulted in the first detailed 3-D maps of crustal thickness and Moho transition zone character covering 658 square kilometers of the East Pacific Rise
- Third-order, but not fourth-order ridge discontinuities are associated with changes in the Moho reflection character and/or near-axis crustal thickness
- Mechanism of lower-crustal accretion varies along the investigated section of the East Pacific Rise but the volume of melt delivered to the crust is mostly uniform

Correspondence to:
O. Aghaei,
omid.aghaei@dal.ca

Citation:
Aghaei, O., M. R. Nedimović, H. Carton, S. M. Carbotte, J. P. Canales, and J. C. Mutter (2014), Crustal thickness and Moho character of the fast-spreading East Pacific Rise from 9°42′N to 9°57′N from poststack-migrated 3-D MCS data, *Geochem. Geophys. Geosyst.*, *15*, 634–657, doi:10.1002/2013GC005069.

Received 30 SEP 2013
Accepted 24 JAN 2014
Accepted article online 27 JAN 2014
Published online 18 MAR 2014

Crustal thickness and Moho character of the fast-spreading East Pacific Rise from 9°42′N to 9°57′N from poststack-migrated 3-D MCS data

Omid Aghaei[1], Mladen R. Nedimović[1,2], Helene Carton[2], Suzanne M. Carbotte[2], J. Pablo Canales[3], and John C. Mutter[2]

[1]Department of Earth Sciences, Dalhousie University, Halifax, Nova Scotia, Canada, [2]Lamont-Doherty Earth Observatory, Columbia University, Palisades, New York, USA, [3]Woods Hole Oceanographic Institution, Woods Hole, Massachusetts, USA

Abstract We computed crustal thickness (5740 ± 270 m) and mapped Moho reflection character using 3-D seismic data covering 658 km^2 of the fast-spreading East Pacific Rise (EPR) from 9°42′N to 9°57′N. Moho reflections are imaged within ~87% of the study area. Average crustal thickness varies little between large sections of the study area suggesting regionally uniform crustal production in the last ~180 Ka. However, individual crustal thickness measurements differ by as much as 1.75 km indicating that the mantle melt delivery has not been uniform. Third-order, but not fourth-order ridge discontinuities are associated with changes in the Moho reflection character and/or near-axis crustal thickness. This suggests that the third-order segmentation is governed by melt distribution processes within the uppermost mantle while the fourth-order ridge segmentation arises from midcrustal to upper-crustal processes. In this light, we assign fourth-order ridge discontinuity status to the debated ridge segment boundary at ~9°45′N and third-order status at ~9°51.5′N to the ridge segment boundary previously interpreted as a fourth-order discontinuity. Our seismic results also suggest that the mechanism of lower-crustal accretion varies along the investigated section of the EPR but that the volume of melt delivered to the crust is mostly uniform. More efficient mantle melt extraction is inferred within the southern half of our survey area with greater proportion of the lower crust accreted from the axial magma lens than that for the northern half. This south-to-north variation in the crustal accretion style may be caused by interaction between the melt sources for the ridge and the Lamont seamounts.

1. Introduction

The structure of the oceanic crust formed along the global mid-ocean ridge (MOR) system is simple compared with the continental crust [e.g., *Raitt*, 1956]. However, the nature of mantle melting, melt extraction, and melt delivery to form the oceanic crust has been a subject of considerable research over the past three decades and is still investigated. To address outstanding questions related to crustal accretion, a number of controlled source seismic experiments have been conducted along and across the East Pacific Rise (EPR) from the mid-1970s to mid-1990s [e.g., *Orcutt et al*., 1975; *Herron et al*., 1980; *Detrick et al*., 1987; *Kent et al*., 1993]. These studies imaged a midcrustal reflection that was interpreted to originate from a thin magma sill (<50 m) [e.g., *Kent et al*., 1990] here referred to as the axial magma lens (AML). The AML is detected beneath much of the ridge axis and sits atop the roof of a broader low-velocity volume (5–10 km wide) extending to the base of the crust and into the uppermost mantle [e.g., *Vera et al*., 1990; *Toomey et al*., 1990]. The discovery of the AML contributed to the development of the gabbro-glacier models for crustal formation at fast-spreading ridges [e.g., *Phipps Morgan and Chen*, 1993; *Henstock et al*., 1993; *Chen and Phipps Morgan*, 1996; *Quick and Delinger*, 1993]. In these models, magma is fed directly from the mantle to the AML where partial crystallization occurs. The upper crust is formed by dike injection and lava extrusion, while the lower crust is formed by downward flow of the crystalline residue due to gravitational forces. More recent ophiolite studies [e.g., *Boudier et al*., 1996] suggest that magma can also accumulate on-axis at lower-crust levels and within the Moho transition zone (MTZ) leading to the dual-sill, multiple magma lens and hybrid crustal accretion hypotheses [e.g., *Schouten and Denham*, 1995; *Kelemen et al*., 1997; *Maclennan et al*., 2004]. In these models, which are supported by tomography, seafloor compliance, and multichannel seismic (MCS) studies [e.g., *Dunn et al*., 2000; *Crawford and Webb*, 2002; *Nedimović et al*., 2005; *Canales et al*., 2009], gabbro

crystallization also occurs within the lower crust and a substantial amount of the lower crust is formed in situ.

The MOR system is partitioned into distinct morphological segments over a variety of spatial and temporal scales [e.g., *Macdonald et al*., 1988]. First-order and second-order (large scale) ridge segments, bounded by transform faults and overlapping spreading centers (OSCs), respectively, have been carefully investigated and are thought to be well understood [e.g., *Macdonald et al*., 1984; *Langmuir et al*., 1986]. First-order segments extend for 600 $\pm$ 300 km and persist for $>5 \times 10^6$ years [e.g., *Macdonald*, 1998]. Second-order segments extend for 140 $\pm$ 90 km and persist for 0.5–5 $\times$ 10^6 years [e.g., *Macdonald*, 1998]. However, the nature and origin of small-scale, third-order (50 $\pm$ 30 km) and fourth-order (14 $\pm$ 8 km) ridge segments, which are proposed to last for 10^4-10^5 and 10^2-10^4 years, respectively [e.g., *Macdonald*, 1998], are still largely debated. *Langmuir et al*. [1986], based on a study of lava compositions, and *Macdonald et al*. [1988], based on high-resolution multibeam swath mapping and acoustic imaging, drew similar conclusions about the source of the third-order ridge segmentation ascribing it to melt extraction processes in the upwelling mantle. However, the two studies disagree about the origin of fourth-order ridge segmentation. Unlike *Langmuir et al*. [1986] who suggested mantle-level processes as the origin of fourth-order segmentation, *Macdonald et al*. [1988] suggested that pinching and swelling of the AML and underlying crustal low-velocity zone causes the finest-scale segmentation. From major and minor analysis of glass samples, *Sinton et al*. [1991] drew similar conclusions to *Langmuir et al*. [1986] and *Macdonald et al*. [1988], inferring that the third-order segment boundaries arise from processes occurring in the mantle. However, some fourth-order segment boundaries are not geochemical boundaries supporting an upper crustal origin [e.g., *Sinton et al*., 1991; *Reynolds et al*., 1992]. Like *Sinton et al*. [1991] and *Reynolds et al*. [1992], but based on the study of along-strike axial hydrothermal activity, *Haymon et al*. [1991] proposed that the origin of fourth-order segmentation is within the upper crust and related to diking processes. Results from more recent high-resolution near-bottom sonar and camera studies by *White et al*. [2002] suggest that the third-order segmentation defines the primary volcanic segmentation of the ridge axis while the fourth-order segmentation seems to be controlled by diking in the upper crust, as proposed by *Sinton et al*. [1991] and *Haymon et al*. [1991].

Controlled source seismic studies of the crust and upper mantle were employed to image ridge structures at depth and address the ambiguity of the origin of small-scale segmentation. Results from tomography studies done by *Dunn et al*. [2000] and *Toomey et al*. [2007] indicate that the origin of both fourth-order and third-order segmentation, respectively, is related to the dynamics of melt generation and transport from the mantle, in agreement with *Langmuir et al*. [1986]. From interpretation of 2-D MCS data, *Carbotte et al*. [2000] show that there is also linkage between fourth-order tectonic segmentation and upper crustal magma plumbing system. The causal relationship between the structure of the midcrustal magma reservoir and small-scale segmentation was further tested by analysis of high-resolution reflection images of the AML from Siqueiros to Clipperton Transform using modern swath 3-D MCS data [*Carbotte et al*., 2013]. This study showed that the crustal magma body is partitioned into segments 5–15 km long coinciding with the fourth-order ridge segmentation further confirming the linkage between this tectonic segmentation and the upper crustal magma plumbing system.

Here we hypothesize that MTZ character and crustal thickness reflect the style of crustal accretion, and that the mode of accretion can vary along axis possibly from one small-scale ridge segment to another. Multiple magma body accretion models call for magma sills within the MTZ suggesting a thicker and more complex crust-mantle transition than that associated with the gabbro-glacier model. If melt extraction processes in the upwelling mantle contribute to the origin of the small-scale ridge segmentation, as proposed by most authors for the third-order and by some for the fourth-order segmentation, then it is possible that the variations in the melt delivery between adjacent segments are also reflected in variations in the MTZ character and crustal thickness. To test this, we carry out a detailed analysis of the crustal thickness and the MTZ character along the EPR from 9°42′N to 9°57′N. For this analysis, we use a state-of-the-art 3-D MCS data set acquired in summer 2008 on *R/V Langseth* and covering 714 km^2 [*Mutter et al*., 2009]. This is the first full, multisource and multistreamer 3-D MCS data set collected over a MOR environment. Examination of the formed high-resolution 3-D reflection cube provides new constraints and insights on the crustal thickness, fine-scale ridge segmentation, and style of crustal accretion along this section of the EPR.

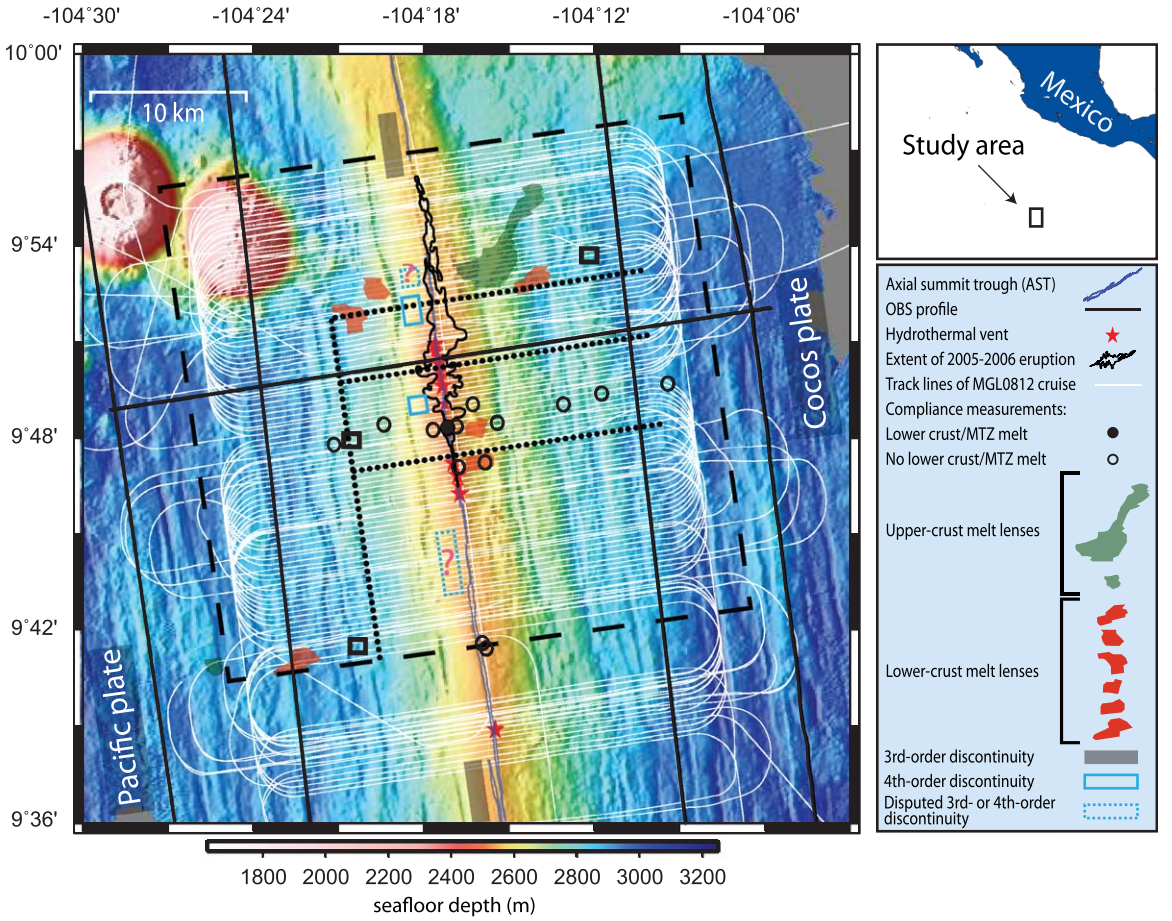

Figure 1. Ship track for cruise MGL0812 is shown using thin white lines superimposed over the EPR bathymetry (color background) between 9°36′N and 10°N latitude. Dashed box outlines the extent of the area of 3-D MCS coverage analyzed for this study. Three open black squares show the location of the CMP supergathers presented in Figure 3. Dotted lines show the surface trace of inlines and crosslines from the 3-D migrated stack presented in Figure 4. Solid lines are OBS profiles from the 1997 UNDERSHOOT experiment [*Toomey et al*., 1997]. Hydrothermal vent locations are from *Haymon et al*. [1991] and the Marine Geoscience Data System (http://www.marinegeo.org/tools/search/targets.php?id=EPR). Axial summit trough (AST) is as interpreted by *Soule et al*. [2007] and is available at http://www.marinegeo.org/tools/search/Files.php?data_set_uid=17147. Extent of 2005–2006 eruption is from *Soule et al*. [2009]. Compliance measurements (circles) are from *Crawford and Webb* [2002]. Third-order segment boundaries are shown with filled gray rectangles; fourth-order segment boundaries are shown with open blue rectangles; debated third-order and fourth-order segment boundaries are shown with dashed blue rectangles. Locations of discontinuities are from *Haymon et al*. [1991], *White et al*. [2002, 2006], and *Carbotte et al*. [2013]. Off-axis magma lens locations are from this study.

2. Study Area

Located in the Pacific Ocean about 900 km southwest of Mexico, the study area covers the fast-spreading EPR (11 cm/yr full rate) [*Carbotte and Macdonald*, 1992] between 9°42′N and 9°57′N (Figure 1). In the east-west direction, the survey extends on both ridge flanks out to about 10 km away from the ridge axis, or to crustal ages of ~180 Ka.

The study area represents a part of the second-order EPR segment that is bounded to the south by the OSC at ~9°03′N and to the north by the Clipperton transform fault at ~10°10′N [*Macdonald et al*., 1984, 1992], which are second-order and first-order ridge discontinuities, respectively. Within the study area, a third-order discontinuity is identified extending from 9°56′N to 9°58′N [e.g., *White et al*., 2006], as well as a number of smaller discontinuities including one at 9°43′N–9°45′N that has been variously interpreted as a third-order or fourth-order offset [*White et al*., 2002, 2006]. Other fourth-order discontinuities have been identified at ~9°49′N and ~9°51.5′N [*Haymon et al*., 1991; *White et al*., 2002, 2006; *Haymon and White*, 2004; *Carbotte et al*., 2013]. *White et al*. [2006] provide an alternative location of the fourth-order discontinuity centered at 9°51.5′N at 9°53′N.

An axial midcrustal magma lens is identified for most of the length of the EPR from the OSC at 9°03′N to the Clipperton transform, suggesting that the whole area is an active magmatic system [e.g., *Kent et al*.,

1993]. Nevertheless, a third-order discontinuity at 9°37′N [*Smith et al*., 2001], just south of our study area, appears to mark a magmatic and hydrothermal boundary. Based on axis-centered studies of lava chemistry, lava age, and volcanic morphology, it is suggested that the ridge north of this discontinuity has recently been (last 5 ka or so) more volcanically active than its southern counterpart [*Smith et al*., 2001]. This section of the EPR north of 9°37′N is characterized by a broad axial cross-sectional area, shallower ridge axis, numerous hydrothermal vents and the presence of a bright and shallow midcrustal axial magma body, all of which have been interpreted as indicative of high magma budget [*Scheirer and Macdonald*, 1993; *Macdonald et al*., 1984; *Haymon et al*., 1991; *Detrick et al*., 1987]. Seafloor volcanic eruptions occurred in 1991–1992 [*Haymon et al*., 1993] and 2005–2006 [*Tolstoy et al*., 2006] coincident with the shallowest region along the ridge axis which is located between 9°48′N and 9°50′N and erupting higher Mg# (hotter temperature) lavas than the regional trend, further suggesting increased magma volume/presence in this region of the EPR [*Batiza and Niu*, 1992].

Two-dimensional MCS experiments conducted from the early 1980s to mid-1990s [*Herron et al*., 1980; *Detrick et al*., 1987; *Harding et al*., 1993; *Kent et al*., 1993] over the EPR between 9°N and 10°N resulted in images of a narrow midcrustal AML (about 0.5–1.2 km wide and 10–50 m thick) [e.g., *Kent et al*., 1993] that resides 1.4–1.9 km below the seafloor. Extreme values of 0.25 and 4 km for the width of AML are found outside our 3-D box, at ∼9°35′N and ∼9°18′N, respectively [*Kent et al*., 1993]. MTZ melt accumulations have been identified from compliance measurements (Figure 1) at 9°48′N [*Crawford and Webb*, 2002]. Intracrustal off-axis magma lenses (OAMLs) have also been reported in our study area (Figure 1) [*Canales et al*., 2012] using a subset of the 3-D MCS data analyzed for this work. The investigators interpret intracrustal reflection events as indicative of partially molten OAMLs based on both MCS and ocean bottom seismometer (OBS) data. The MCS data show reversed polarity for the OAML events, just as they do for the midcrustal AMLs, indicating a negative impedance contrast. The OBS data show high attenuation of seismic arrivals that travelled through the crust where OAMLs occur. The OAMLs described by *Canales et al*. [2012] are found in the upper crust from 9°52.5′N to 9°56′N and located 5.5–7 km east of the ridge axis at depths of 2.1–2.3 km below seafloor (bsf). A deeper OAML, found in the same area at 4.2 km below the igneous basement, has also been described by *Canales et al*. [2012].

Velocity and thickness of seismic layer 2A, the shallowest part of the igneous oceanic crust, have been determined in the study area and surrounding regions by the same 2-D MCS data used to study the AML and crust in general [e.g., *Harding et al*., 1993], but also from near-bottom refraction data [e.g., *Christeson et al*., 1992], OBS tomography [e.g., *Toomey et al*., 1990; *Tian et al*., 2000; *Sohn et al*., 2004], and expanding spread profile (ESP) refraction studies [*Vera et al*., 1990]. Based on the 1-D models derived from on-axis ESP experiments from 9°32′N to 9°35′N, the *P*-wave velocity of the uppermost (100–200 m) crust is low (<2.5 km/s) and increases rapidly to ∼5 km/s at ∼500 m below the seafloor [*Vera et al*., 1990]. The 2-D MCS data from 9°40′N to 9°50′N show that the thickness of layer 2A varies from ∼250 m at the ridge axis to >500 m at places away from the ridge axis [*Harding et al*., 1993]. Based on this MCS study, the average layer 2A thickness in our study area and up to a distance of 10 km away from the axis is ∼460 m. Asymmetric cross-axis velocity of layer 2A, with the velocities on the western flank lower than on the eastern flank, is observed at 9°50′N from OBS data [*Tian et al*., 2000]. An OBS refraction experiment conducted at 9°50′N using near-bottom sources [*Sohn et al*., 2004] further constrains the fine-scale seismic structure of layer 2A. This low-velocity layer (*P*-wave velocity and *S*-wave velocity of 2.20 and 0.42 km/s, respectively), made of extremely porous lava and basalt breccia, has a thickness that increases systematically from ∼20 m on the rise axis to ∼120 m at a distance of ∼1.5 km to the east and ∼0.5 km to the west of the ridge axis.

Two-dimensional MCS data collected over young oceanic crust contain a prominent reflection at about 2 s two-way traveltime (TWTT) below the seafloor that is interpreted as the Moho reflection event [e.g., *Stoffa et al*., 1980; *Herron et al*., 1980; *Barth and Mutter*, 1996]. Seismic modeling of this event shows that the Moho is not a single discontinuity but rather a transition zone (MTZ) with both positive velocity gradients and varying thicknesses [*Vera et al*., 1990]. Seismic profiling carried out along the EPR at 14°S shows that, where the Moho reflection response is imaged, the seismic character of Moho varies from impulsive, to shingled, or diffusive [*Kent et al*., 1994]. This spatial and temporal variability of the Moho reflection response was interpreted to be caused by a heterogeneous interface between the crust and the mantle. A similar pattern for the Moho reflection response was identified within the 8°50′N to 9°50′N EPR area [*Barth and Mutter*, 1996].

The thickness of the igneous crust for the 8°50′N to 9°50′N area has been computed by *Barth and Mutter* [1996] using 2-D MCS data and for the area between the Clipperton and Siqueiros transform faults by *Canales et al*. [2003] using OBS data. The computed thickness based on reflection profiles spaced about 3.5 km apart and a few 1-D ESP velocity models of *Vera et al*. [1990] was done for crust up to ∼300 Ka old. The results show that the crustal thickness variation for the 8°50′N to 9°50′N latitude range is ∼2.6 km, with the thinnest crust at 5–5.5 km between ∼9°40′N and 9°50′N and the thickest crust 7–7.3 km immediately north of the OSC between 9°15′N and 9°20′N. The crust gradually thickens to the south between these two locations, and then thins south of 9°15′N–9°20′N to ∼6.5 km at 8°50′N. The majority of this crustal thickness variation was attributed to layer 3.

The crustal thickness between 8°15′N and 10°10′N (Siqueiros and Clipperton transform faults, respectively), computed by simultaneous inversion of OBS refraction and wide-angle Moho reflection arrivals [*Canales et al*., 2003], is based on four ridge-parallel profiles evenly distributed on each side of the ridge axis and two ridge-perpendicular velocity profiles. Two of the ridge-parallel profiles are located on ∼150 Ka old crust and the other two velocity profiles are located on ∼300 Ka old crust. The ridge-perpendicular velocity profiles at ∼8°35′N and ∼9°15′N are ∼75 km apart. The computed mean crustal thickness between the Siqueiros and Clipperton fracture zones is 6.7–6.8 km. The crust thickens away from the Siqueiros and Clipperton transforms, to the north and south, respectively, reaching maximum thickness of 7.3–7.8 km north of the 9°03′N OSC at 9°15′N, about midway between the transforms. This excludes measurements over seamounts where the crust can be anomalously thick. The thinnest crust (5.3 km) is found within the Siqueiros transform. From 9°15′N to 9°50′N, the OBS results show a smaller crustal thickness variation (1.3–1.8 km) than inferred for this same area from 2-D MCS data (2.3 km) [*Barth and Mutter*, 1996]. For the area investigated in our study, the mean crustal thickness to crustal age of 300 Ka is ∼5.5 km based on the 2-D MCS results [*Barth and Mutter*, 1996] and to crustal age of 225 Ka is ∼6.8 km based on the OBS data [*Canales et al*., 2003].

3. Data

3.1. Data Acquisition

In summer of 2008, we conducted a 3-D MCS survey over the EPR between 9°35.6′N and 9°57′N onboard *R/V Marcus Langseth* during expedition MGL0812. Two areas of 3-D coverage separated by a 3.3 km gap were acquired. The larger northern area (∼714 km^2) that is investigated in this study is located between 9°42′N and 9°57′N (Figure 1). This area is covered with 94 primary, 11 infill, and 10 reshoot sail lines. Sail lines are 24 km long, separated by 300 m, and have an azimuth of 82° from North. Four 6 km long hydrophone streamers separated by 150 m were towed at a depth of 10 m along sail lines. Each streamer was composed of 468 receiver-array groups spaced every 12.5 m, for a total recording of 1872 channels per shot. Recording time was 10,240 ms and sample rate was 2 ms. Two seismic sources, each comprised of two linear arrays of nine air guns with a total volume of 3300 in^3 were towed at a depth of 7.5 m. The two sources were fired in an alternating (flip-flop) mode every 37.5 m resulting in eight common midpoint (CMP) profiles per sail line. These CMP lines are separated by 37.5 m. The total number of shots fired in the northern area is 73,737 and total number of data traces recorded is 138,053,664. Shot and receiver positions were determined with a 1 and <3 m horizontal accuracy, respectively, through analysis of global positioning system (GPS), acoustic transponder, and streamer compass information.

The geometry of the survey yields CMP bins that are 37.5 m wide and 6.25 m long in cross along-ridge-axis and cross-ridge-axis directions, respectively. To achieve full nominal fold of 40 traces per CMP bin for the central 16 km wide area about the ridge axis (∼451 km^2), sail lines included 4 km run-in and run-out. Nevertheless, fold distribution deviated from the nominal value due to streamer feathering, survey gaps caused by marine life, and technical shutdowns. The average feathering was ±5° requiring minimal infill. Gaps in the survey due to marine life and technical shutdown were minimized with reshoot lines. Additional details on data acquisition are given in *Mutter et al*. [2009].

3.2. Data Analysis

The survey geometry is developed by using shot and receiver locations to compute true source-receiver offsets and midpoint positions for all seismic data traces. The data traces are then assigned to nominal 37.5 × 6.25 m CMP bins. The prestack processing sequence applied to the data starts with bandpass filtering (1–6–

200–220 Hz) and frequency spectrum balancing, both 1-D processes, and continues with 2-D filtering of shot gathers. Both filters are used to remove ambient and low-frequency cable-tow noise. The frequency spectrum balancing is applied only to the low-frequency range from 0 to 14 Hz to remove a spike with peak frequency between 4 and 6 Hz.

For 2-D filtering, we evaluated the effectiveness of available algorithms by first computing a synthetic shot gather in the frequency domain using a finite-difference solution of the acoustic wave equation [*Pratt and Worthington*, 1990]. A *P*-wave velocity and density model for the EPR is required for this process. We used a 1-D hybrid velocity model that includes (a) a velocity-depth variation from seafloor to AML from the ESP5 velocity function of *Vera et al*. [1990]; (b) a linear velocity gradient layer to model layer 3 starting from 5.5 km/s just below the AML and increasing to 6.5 km/s at the Moho; and (c) a step velocity function of 8 km/s to model mantle. This velocity model resulted in both AML and Moho reflections, which allowed us to test the effectiveness of available 2-D filters at different traveltimes and signal-to-noise (S/N) ratios. A minimum phase Keuper wavelet with a bandwidth from 0 to 50 Hz was used as the source function in this test. Pure ambient and streamer noise recorded during the data acquisition were added to the modeled shot gather to simulate a typical shot gather for the survey.

Test results on this shot gather show that the LIFT method [*Choo et al*., 2004], simplified so as not to include the signal-add-back step, removes noise efficiently without taking out signal. Because much of the dominant low-frequency cable noise is in the 0–15 Hz range, the shot gathers were divided before filtering into low-frequency and high-frequency bands, that is 1 to 10–15 Hz and 15–20 to 220 Hz, respectively, with an intermediate band represented by the difference between the original data and the low-frequency and high-frequency bands. In the simplified LIFT sequence, a frequency-wave number (FK) filter is applied to the low-frequency band of the data to suppress ambient and streamer noise followed by applying a 2-D median filter to all frequency ranges to suppress amplitude spikes. All frequency bands are combined after 2-D filtering to form the filtered shot gathers (Figure 2).

Offset-dependent spherical divergence correction to compensate for geometrical spreading, surface-consistent amplitude balancing to normalize abnormally high/low shot and channel amplitudes, and trace editing follow in the processing sequence. After noise cleanup and amplitude normalization are completed, Moho reflection is in most cases still challenging to identify on individual CMP bin gathers so they need to be combined into CMP bin supergathers. Although visible on many and strong on some CMP supergathers (Figure 3), the Moho reflection on prestack gathers is not strong enough and continuous enough for a systematic normal moveout (NMO) velocity analysis. Therefore, three 3-D velocity models were developed for stacking the data by hanging existing 1-D velocity functions from the seafloor. The stack volumes produced in this way are based on the ESP5 function [*Vera et al*., 1990] determined from axial data, the ESP1 function [*Vera et al*., 1990] determined using data collected ~10 km off the axis, and cross-axis OBS velocity profile at 9°50′N [*Canales et al*., 2012]. Common midpoint bin gathers were then NMO corrected, stretched far offset arrivals were muted, and these gathers were summed to form stacked 3-D image volumes. The maximum offset used in CMP bin gathers for stacking the AML event was ~2.7 km and the maximum offset range that resulted in the best overall image for Moho event was 4.5 km. Stacking the full offset range of CMP bin gathers (~6 km) at Moho level led to poorer images of the Moho reflection at some locations likely because the velocity models did not fully flatten this event. The 3-D stack volume produced using the ESP1 velocity function provided the best overall image of all structures, including the AML, despite the velocities being extracted from off-axis data.

Poststack processing included a seafloor multiple mute to reduce migration noise followed by 3-D Kirchhoff poststack time migration. The 3-D migration velocity model was produced by hanging from the seafloor the 1-D ESP1 velocity function of *Vera et al*. [1990] and converting it to RMS velocity. Time-variant band-pass filtering and time-variant balancing were applied to the migrated stack volume (Figure 4). For imaging the layer 2A/2B boundary, the prestack processing is identical up to the velocity analysis. Normal moveout velocities that flatten the retrograde part of 2A refraction are then chosen and the data are again stacked using 1600–3550 m offset range. Stacking velocity for layer 2A gradually increased from 1580 m/s on the ridge axis to some 100 m/s higher stacking velocity on the ridge flanks, at the outer edge of the 3-D volume. The layer 2A 3-D stack volume was migrated in the inline and crossline directions and unwanted parts of the new image volume were zeroed to extract only the layer 2A event.

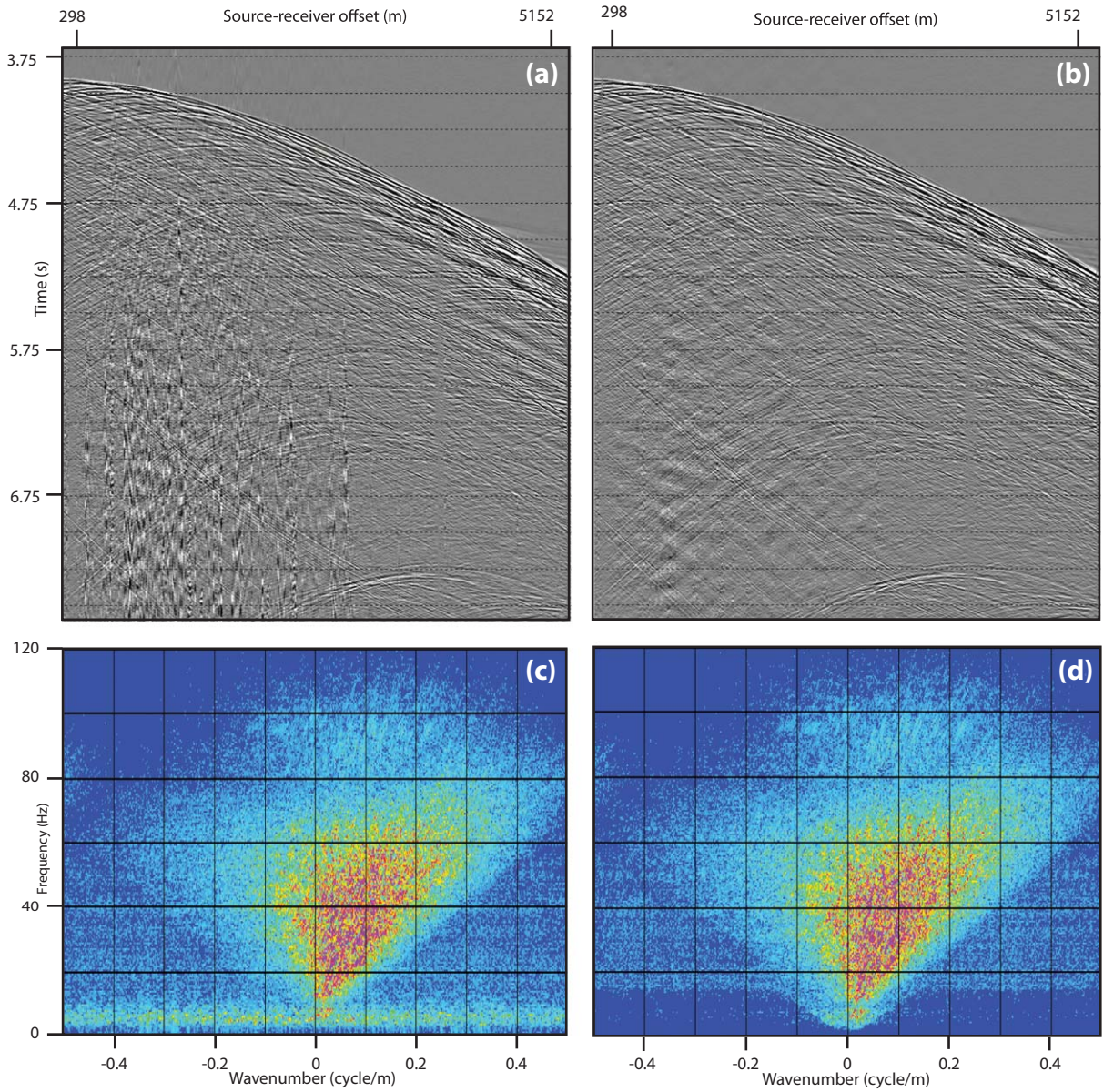

Figure 2. Noise suppression on shot gathers by application of simplified LIFT method. (top) Shot gather (a) before and (b) after LIFT. (bottom) Frequency-wave number spectra (c) and (d) correspond to data shown in (a) and (b), respectively. Frequency-wave number spectrums in (c) and (d) are shown only for frequencies of up to 120 Hz because most of the signal is found within this range and most of the removed noise has frequencies of $<$10 Hz. Level of streamer and ambient noise is high as this shot is recorded when turning onto a sail line.

4. Results

The primary result of this work is a 714 km^2 3-D migrated stack volume of the EPR between 9°42′N and 9°57′N, of which some 658 km^2 are considered to have satisfactory S/N ratio for interpretation because of the sufficiently high CMP bin fold and even offset distribution. This 3-D image volume allows for detailed mapping of the seafloor and MTZ reflections (Figure 4), which are needed for the study of the MTZ character and crustal thickness presented here. To facilitate the discussion, we also pick the layer 2A/2B boundary and map on-axis and off-axis magma lenses. However, detailed analysis of the AML, OAMLs, and layer 2A are beyond the scope of this work and will be presented in future studies.

4.1. Moho Reflection Response

Moho transition zone reflections are imaged in about 87% of the study area. Where the Moho reflection response is imageable, its strength and character vary spatially both on CMP bin supergathers (Figure 3)

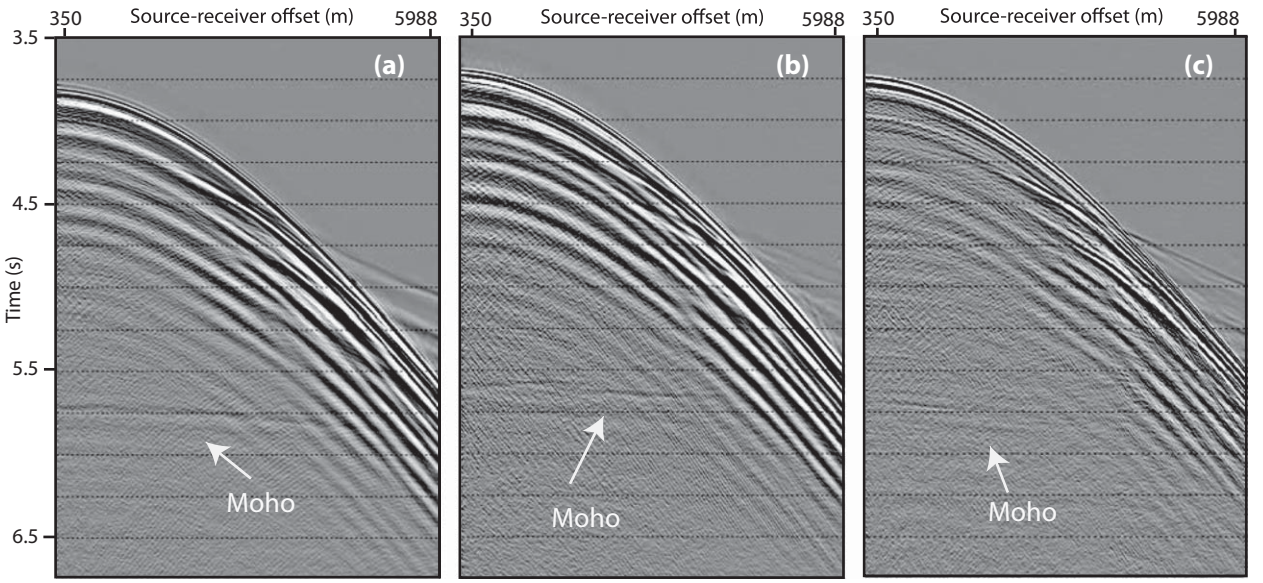

Figure 3. Variations in the Moho reflection strength and character on CMP bin supergathers: (a) strong impulsive Moho; (b) moderate strength impulsive Moho; and (c) moderate strength diffusive Moho. CMP supergathers for the impulsive Moho were constructed ~7 km from the ridge axis on the Pacific plate at (a) 9°42′N and (b) 9°48′N. CMP supergather for the diffusive Moho was constructed at ~10 km on the Cocos plate at ~9°54′N. Note that the Moho reflection strength and character are defined on the migrated stack volume and that the shingled Moho has the same appearance on CMP supergathers as the impulsive Moho. Where the Moho reflection is weak in the stacked volume, it is not visible on CMP supergathers. For creating CMP supergathers at impulsive and shingled Moho areas, CMP bin data around the target gather and common to 40 inlines and 200 crosslines were combined. This means that CMP bin data from 1250 × 1500 m area were presented as one large gather. Number of crosslines used at diffusive area was reduced to 50 because of the more rapid spatial variation of the reflection response of a diffusive Moho that results in negative interference and cancelation of the signal.

and migrated stack images (Figures 4 and 5). In terms of the Moho reflection response amplitude, we differentiate in a qualitative way between strong, moderate, weak, and absent Moho. This amplitude differentiation of the Moho reflection response was designed on and applies to the 3-D migrated stack (Figures 4 and 5), but does not apply to the CMP bin supergathers (see Figure 3). In terms of the Moho reflection response character, we differentiate similar to *Kent et al*. [1994] between impulsive, shingled, and diffusive.

Thin MTZs are thought to generate the impulsive and shingled Moho reflection responses [*Brocher et al*., 1985; *Collins et al*., 1986; *Nedimović et al*., 2005]. Both the impulsive and shingled Moho types are single-phase reflection responses. The difference is that the impulsive Moho response is continuous and shingled Moho response is broken in smaller sections that are vertically offset and can overlap. Where the single-phase Moho is composed of overlapping segments that resemble roof shingling (e.g., Figure 5), overlap between individual segments can be as large as 500–1000 m. This overlap does not represent real structure but rather a migration artifact caused by using full crustal velocities for migration, which at these depths are high and can cause lateral smearing but are needed to fully collapse any diffractions. Images produced using reduced migration velocities do not exhibit lateral smearing and vertically offset Moho reflection segments do not overlap. Thick MTZs are believed to generate the diffusive Moho type [*Brocher et al*., 1985; *Collins et al*., 1986; *Nedimović et al*., 2005], which is characterized by a multiphase reflection response.

The MTZ reflection strength and character, identified visually and assigned manually to each trace, including pick uncertainty, are summarized for the whole study area in Figure 6. Strong Moho reflections are imaged within 39%, moderate within 25%, and weak within 23% of the study area (Figure 6a). Spatial distribution of on-axis and off-axis magma lenses is closely associated with the regions where no Moho reflections can be recognized, which cover some 7% of the study area. The challenge of imaging structures below or in the vicinity of magma lenses has long been known with only one study claiming to have imaged Moho reflections beneath the ridge axis [e.g., *Singh et al*., 2006]. Areas with magma strongly attenuate and disperse seismic energy to the point that it still remains unclear at which age the reflection Moho forms. In the *Kent et al*. [1994] and *Barth and Mutter* [1996] studies of the EPR, Moho was imaged within 1–2 km from the AML edge. With the standard processing sequence applied, Moho reflections were not imaged anywhere below the ridge axis. However, our results show that the distance from the ridge axis at which the Moho reflections become weak and disappear varies with latitude. From ~9°42′N to ~9°48.5′N and

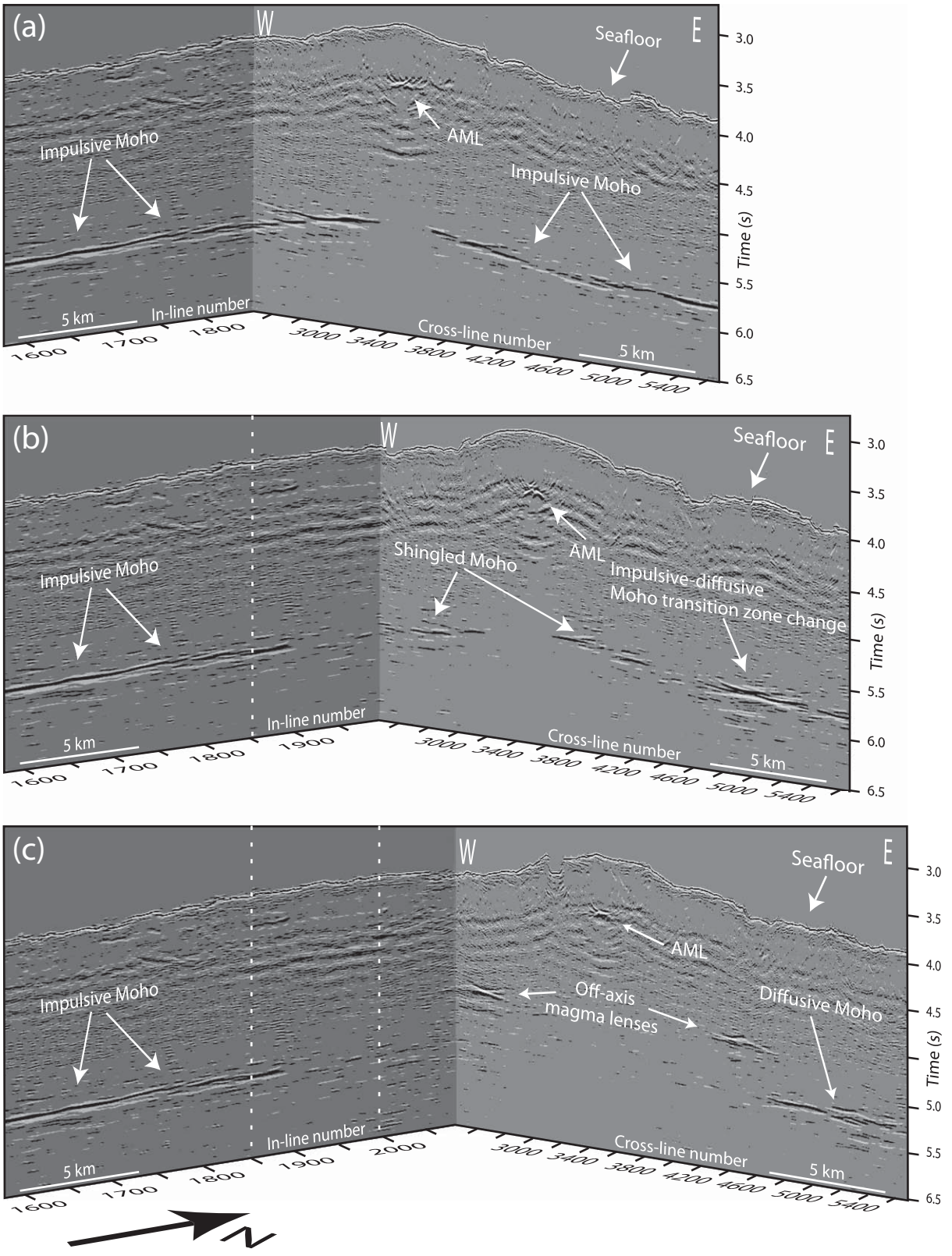

Figure 4. Seismic images from the 3-D migrated stack volume showing reflection responses from the seafloor, AML, OAMLs, and Moho. Also visible in the first second of crustal TWTT and at lower amplitudes are low-frequency (~5 Hz) reverberations most likely representing the residual bubble pulse. All three images feature the same crossline (2500) and a different inline which, from south to north, are (a) 1850, (b) 1990, and (c) 2090. Note the remarkable clarity of the Moho and other recorded reflections, as well as the variation in the Moho reflection response from impulsive in the south to diffusive in the north. Inlines are 37.5 m separated CMP lines in the sail line (~ENE) direction. Crosslines, separated 6.25 m, are perpendicular to the inlines.

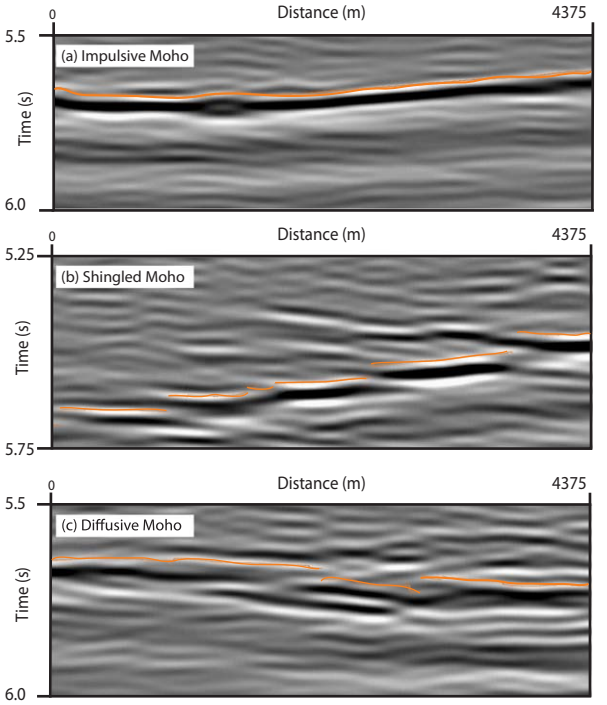

Figure 5. Zoom on the types of Moho reflection responses in the study area (a) impulsive, (b) shingled, and (c) diffusive. Orange lines show the Moho reflection arrival picks.

from ~9°53′N to ~9°57′N, the Moho reflection is imageable until about 450 m from the ridge axis. The Moho reflection gap beneath the ridge axis increases to ~1050 m from ~9°48.5′N to ~9°50′N and to 2400 m from ~9°50′N to ~9°52.5′N on the Pacific plate and 1250 m on the Cocos plate. For ~1 km along-axis distance north of ~9°52.5′N, Moho reflections cannot be imaged on the Cocos plate until ~5 km away from the axis. The last two areas described, covering from ~9°50′N to ~9°53′N, show asymmetry between the opposing flanks in terms of the distance from the ridge axis at which Moho reflections become imageable. The only region away from the ridge axis where Moho reflections are not imaged lies between ~9°50′N and ~9°56′N (Figure 6a), where the largest and most abundant OAMLs are concentrated (Figure 1).

Impulsive MTZ reflection response is imaged within 41%, shingled within 29%, and diffusive within 17% of the study area (Figure 6b). The map in Figure 6b was formed by, for the purpose of this study, assuming that if the Moho reflection response is single-phase and continuous for ≥2 km, the Moho type is impulsive. If the Moho reflection response is single-phase and segmented by vertical offsets into sections ≤2 km long, the Moho type is shingled. All multiphase MTZ reflection responses are representative of the diffusive Moho type. Figure 6c shows the uncertainty in Moho reflection picks, which was assigned visually during the picking process. More than half of the area where Moho reflections are imaged (46% of the study area) has picks of low (16 ms) uncertainty, with smaller portions represented with medium (66 ms) and high (116 ms) uncertainty (24% and 17% of the study area, respectively). A substantial portion of the high uncertainty picks is from the edges of the picked area, where migration can produce lateral smearing of the Moho reflection signal.

From ~9°42′N to ~9°48′N on the Pacific Plate, Moho reflection response appears as an impulsive single-phase event that dips away from the ridge axis. Reflection strength and S/N ratio are high and the Moho reflection is easy to identify. The Moho reflection is continuous in segments >3 km with small (<150 m) disruptions between them. Moho reflection picks have a low uncertainty in this latitude range. From ~9°48′N to ~9°56′N on the Pacific plate, Moho reflection character differs markedly from the reflection character further south. From ~9°48′N to ~9°50′N, Moho reflection changes from a continuous, single-phase event to vertically offset and overlapping discontinuous event with segments ≤2 km long, which we interpret as shingled Moho. At some locations, because of lower S/N ratio and overlapping segments, Moho picks are of higher (moderate) uncertainty. Further north on the Pacific plate (~9°50′N to ~9°56′N), seismic character of the Moho response changes from a single-phase event to a multiphase event, and the reflection strength weakens. The Moho reflection response is also disrupted at intervals sometimes <1 km. This area is characterized by the highest pick uncertainty. The area from ~9°56′N to ~9°57′N, at the northern edge of the 3-D box, appears to be transitional with the Moho reflection response returning to mostly shingled and impulsive. However, the reflection strength and S/N ratio are variable and pick uncertainty is mostly high.

Moho reflection amplitudes are weaker and more variable across the ridge axis on the Cocos plate. The Moho reflection response alternates between shingled and impulsive from ~9°42′N to ~9°52′N, with the shingled Moho occurring closer to the ridge axis at ~9°42′N to ~9°43.5′N and from ~9°50′N to ~9°52′N, and the impulsive Moho appearing some 6 km away from the axis. Where shingled, Moho reflection

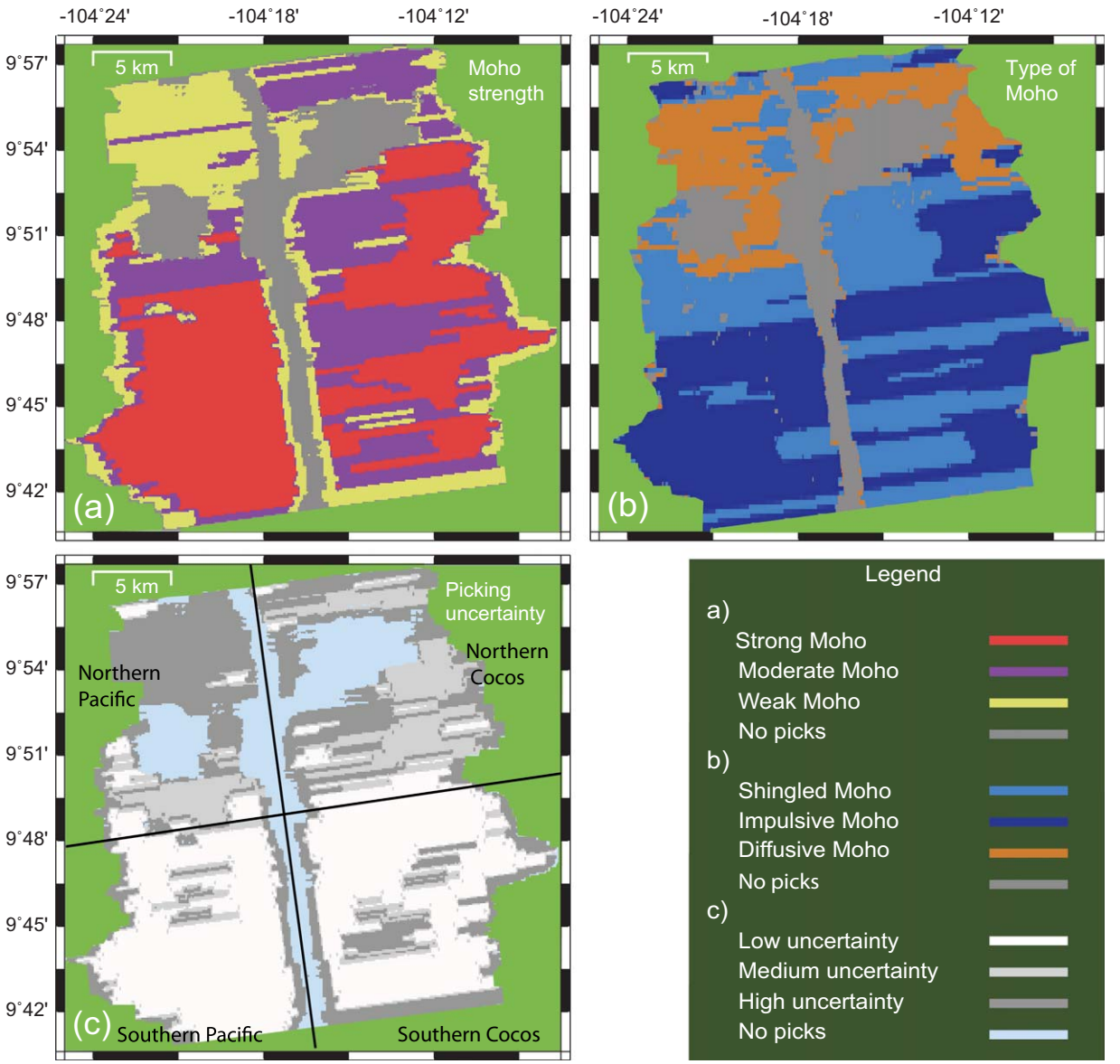

Figure 6. MTZ reflection response maps showing: (a) Moho reflection strength, (b) Moho reflection type, and (c) pick uncertainty. These maps were formed by analysis of inlines and crosslines extracted from the 3-D migrated stack volume at every 300 and 150 m, respectively. Thin black crossing lines in Figure 6c divide the study area into northern Cocos, northern Pacific, southern Pacific, and southern Cocos quadrants. Position of the latitude for separating the north and south quadrants is chosen to coincide with a major change in the Moho reflection character.

strength is mostly lower and picking uncertainty mostly higher. From ~9°52′N to 9°55′N, Moho reflections are in large part not traceable, and where they are the MTZ reflection response is diffuse. From ~9°55′N to 9°57′N, Moho seismic character changes back from diffusive to impulsive.

4.2. Crustal Thickness

Figure 7 shows maps of (a) Moho reflection TWTT, (b) seafloor to Moho reflection TWTT or crustal TWTT, (c) velocity at 6 km depth below the seafloor, and (d) crustal thickness. A minimum curvature method was used for creating the gridded maps. These maps cover some 87% of the study area, which corresponds to the percentage of the area where the MTZ reflections are imaged. Moho TWTTs were picked manually in great detail, on all traces (6.25 m spacing) of every other inline (every 75 m) of the 3-D migrated stack volume. The first negative break of the energy reflected from the Moho was chosen for picking. Because the air gun array produces a minimum phase wavelet and the marine MCS acquisition equipment is calibrated so that the first arriving energy on the records has negative amplitudes, this picking increases the true

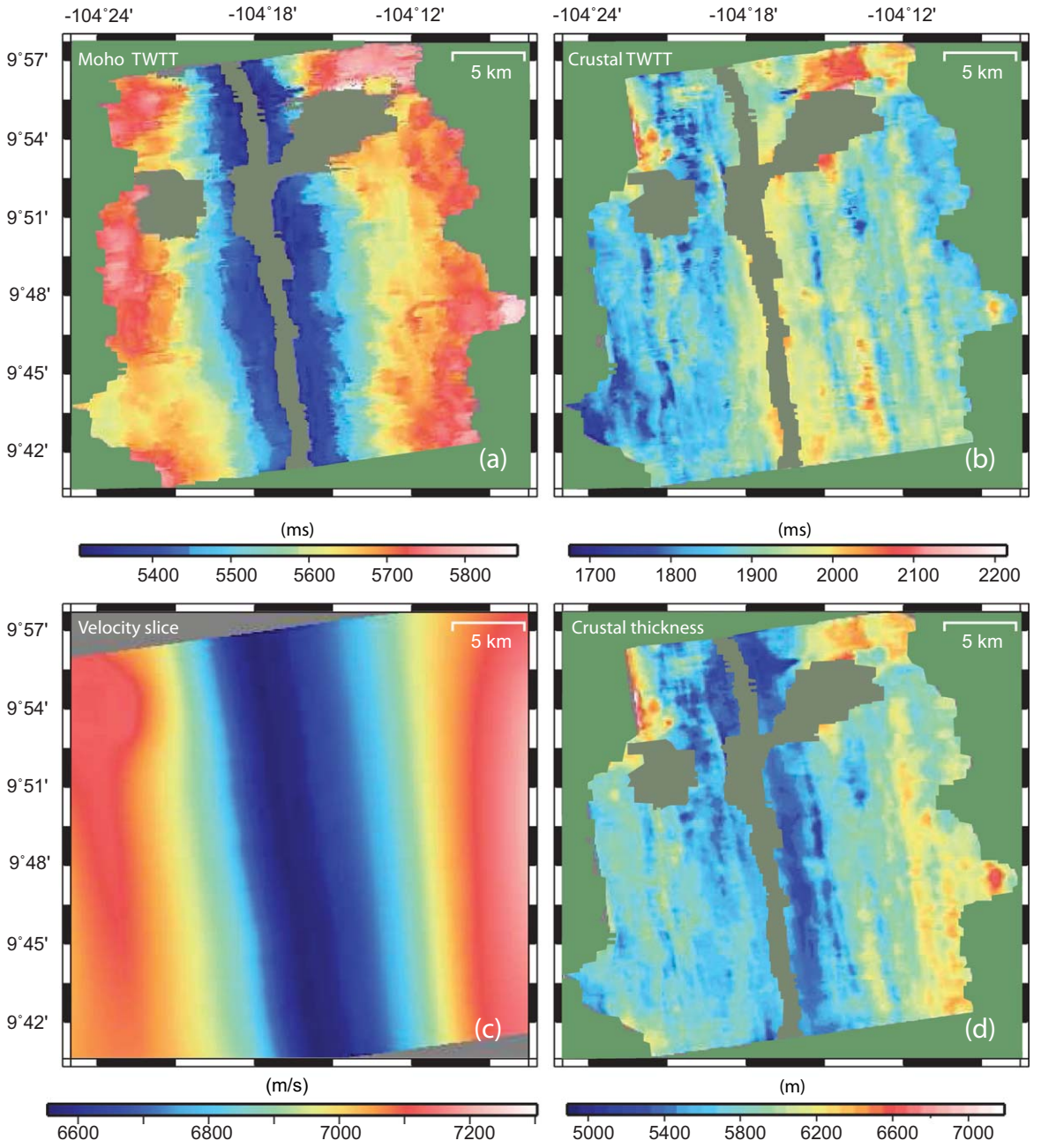

Figure 7. Crustal thickness variation in the study area: (a) Moho reflection TWTT map; (b) crustal TWTT map; (c) velocity at 6 km depth below the seafloor; (d) crustal thickness after converting smoothed TWTT values to depth using the velocity model shown in Figure 7c and developed from the OBS profiles (Figure 1). These maps were formed by interpolating and extrapolating the picked Moho reflection response information for up to 700 and 350 m between and away from the data points, respectively.

crustal TWTTs by ~18 ms, which is equivalent to the delay from the onset of arriving energy to the first negative peak. To reduce this picking-related increase in crustal TWTTs, the first negative break for the seafloor reflection arrival was also picked introducing a similar delay of ~5 ms. The magnitude of the two delays is different because of the different frequency spectrums of the signal at the top of the igneous basement and at the MTZ (i.e., dominant signal frequencies of ~50 and ~14 Hz, respectively). When subtracted, the two delays yield 13 ms difference, or ~41 m assuming average crustal velocity of 6250 m/s. This systematic error in measured crustal TWTTs was removed.

Figure 7b shows that the largest variation of crustal TWTTs is in the across-axis direction, along the flow lines, and that the smallest variation of TWTTs is in the axis-parallel direction, along the isochrons, forming

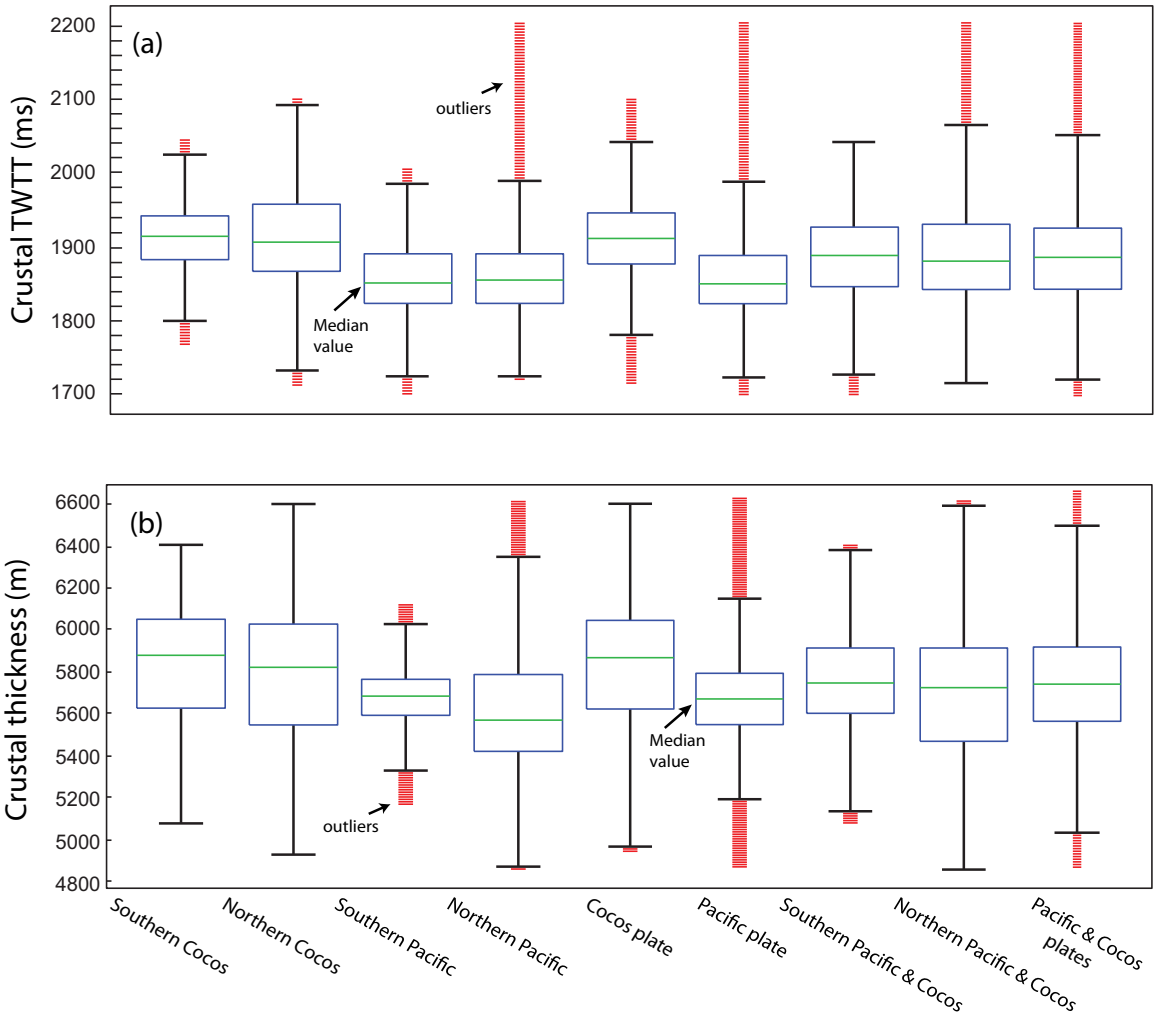

Figure 8. Box plots of (a) crustal TWTT and (b) crustal thickness for plate quadrants shown in Figure 6c, combination of them, and the entire study area. On each box, the central green line marks the median (Q2) value and the upper and lower edges of the blue box are 25th and 75th percentiles or quartiles Q1 and Q3, respectively. The whisker length, from Q3 + 1.5(IQR) to Q1 − 1.5(IQR) and corresponding to $\sim\pm 2.7\sigma$, extends to the most extreme data values that are not outliers. Crustal thickness is most variable on northern Cocos plate and it is least variable on the southern Pacific plate. The median crustal thickness on the northern Pacific plate is 260 m smaller than the median crustal thickness on the northern Cocos plate. The difference in median crustal thickness between southern Pacific plate and southern Cocos plate is 180 m where the southern Cocos plate is thicker and the median crustal thickness on the Pacific plate is 190 m smaller than this value on the Cocos plate.

what appears as striping in the along axis direction. A smoothed crustal TWTT map was produced by removing the short wavelength components of the spectrum ($\leq$250 m) from the seafloor TWTT map before subtracting this map from the Moho TWTT map, which lacks the corresponding short wavelengths. For smoothing, we used a locally weighted polynomial regression filter in a 425 m wide and 225 m long window across-axis and along-axis, respectively. After the smoothing, the crustal TWTT map still exhibits the same general features with maximum TWTT variation in the across-axis direction of $\sim$200 and $\sim$100 ms/km in the direction parallel to the ridge axis.

Figure 8a and Table 1 show the results of statistical and error analyses of crustal TWTT data presented in Figure 7b. The statistical and error analyses were carried out for the whole study area, excluding an anomalous 750 m wide stripe region close to the youngest of the Lamont seamounts (upper left corner in Figure 7), as well as for each of the two flanks, and for the study area divided (shown in Figure 6c) into northern and southern Pacific and Cocos plate quadrants. Figure 8a shows box plots of crustal TWTT. Each box plot shows the first (Q1), second (Q2, median), and third (Q3) quartile, and the interquartile range (IQR = Q3 − Q1). For each box plot 99.3% of data coverage is considered, with the whisker lengths (Q3 + 1.5(IQR) and Q1 − 1.5(IQR), corresponding to $\sim\pm 2.7\sigma$) defining the outliers [e.g., *Upton and Cook*, 1996]. The data

Table 1. Computed Crustal TWTT Range and Mean With Associated Standard Deviation and Average Propagated Error for the Investigated Section of the EPR, Pacific and Cocos Plates, and Various Parts of the Study Area

Plate Section	Range (ms)	Mean Value (ms)	Standard Deviation (ms)	Average Propagated Error (ms)
Southern Cocos	1770–2040	1910	40	40
Northern Cocos	1770–2100	1910	60	50
Southern Pacific	1700–2010	1860	50	40
Northern Pacific	1720–2200	1860	60	60
Southern Cocos and Pacific	1700–2040	1890	50	40
Northern Cocos and Pacific	1720–2200	1890	70	50
Pacific	1700–2200	1860	50	50
Cocos	1770–2100	1910	50	40
Cocos and Pacific	1700–2200	1890	60	40

without outliers for both plates (99.3% of all crustal TWTTs) fall within a 330 ms time window, with half of the TWTTs (between 25th and 75th percentiles) falling within a 90 ms window. The mean crustal TWTT varies from 1.86 s on the Pacific plate to 1.91 s on the Cocos plate, with the mean crustal TWTT of 1.89 s for the entire study area (Table 1). Computed standard deviation and average propagated error vary little (40–60 ms) for all plate quadrants and their combinations. When combined, the northern and southern quadrants show the same mean TWTT of 1.89 s.

Crustal thickness (Figure 7d) was computed by depth converting the smoothed Moho TWTT and subtracting seafloor depth. The 2-D crustal velocities used for depth conversion were developed by *Canales et al*. [2003, 2012] by simultaneous traveltime tomographic inversion of refraction and wide-angle Moho reflection arrivals recorded on four axis-parallel and one axis-perpendicular OBS profiles (Figure 1) acquired as part of the Undershoot Seismic Experiment [*Toomey et al*., 1998]. The across-axis velocity profile approximately coincides with inline 2003 of the 3-D survey. To constrain the velocity along the ridge axis before interpolation, we used the axis centered 6 km wide portion of this profile and projected this section along the axis every 150 m. The 3-D velocity volume was then constructed by interpolating velocity values at known locations, the 6 km wide strip along the ridge axis and four axis-parallel velocity profiles found at greater distance from the axis, using the minimum curvature method.

Figure 8b and Table 2 show results of statistical and error analyses of computed crustal thickness values presented in Figure 7d. The statistical and error analyses were carried out for the whole study area and its components as described for crustal TWTTs. Figure 8b shows box plots of computed crustal thickness. The computed crustal thickness values without outliers for both plates (99.3% of all crustal thickness values) fall within a 1480 m window, with half of the crustal thickness values (between 25th and 75th percentiles) falling within a 360 m window. The mean crustal thickness varies from 5660 m on the Pacific plate to 5800 m on the Cocos plate, with the mean crustal thickness of 5740 m for the entire study area (Table 2). Computed standard deviation and average propagated error for all plate quadrants and their combinations vary from 130 to 310 m and from 220 to 370 m, respectively.

For error analysis we use the assigned 16, 66, and 116 ms picking error for zones of low, mid, and high uncertainty in determining Moho reflection arrival time (see Figure 6c), respectively, and for seafloor picks we assign 8 ms error. The error for the OBS-derived velocity models [*Canales et al*., 2012] is 200 m/s, and average crustal velocity used 6250 m/s [*Canales et al*., 2003]. The calculated crustal thickness errors vary from 190 to 450 m with mean value of 270 m (Table 2). Error values of 150–250, 250–350, and 350–450 m in crustal thickness cover 50%, 26%, and 11% of the imaged area, respectively.

4.3. Layer 2A Thickness

The layer 2A was picked using guided automatic picking software, followed by manual editing of the automatic picks [*Carton et al*., 2010]. For depth conversion, a layer 2A velocity model symmetric around the ridge axis was applied. The velocity for depth conversion of layer 2A was developed by analyzing CMP supergathers along inline 1476 [*Han et al*., 2011] using JDseis software that permits modeling gradient velocity layers [*Nedimović et al*., 2008]. The layer 2A thickness varies from 107 to 517 m.

4.4. Intracrustal Magma Lenses

On-axis and off-axis intracrustal reflections with wavelet polarity reversed relative to the polarity of the seafloor event (e.g., Figure 4) are interpreted as partially molten magma sills. Spatial distribution of these

Table 2. Computed Crustal Thickness Range and Mean With Associated Standard Deviation and Average Propagated Error for the Investigated Section of the EPR, Pacific and Cocos Plates, and Various Parts of the Study Area

Plate Section	Range (m)	Mean Value (m)	Standard Deviation (m)	Average Propagated Error (m)
Southern Cocos	5080–6400	5830	280	220
Northern Cocos	4940–6600	5790	310	300
Southern Pacific	5170–6120	5680	130	220
Northern Pacific	4804–6610	5620	260	370
Southern Cocos and Pacific	5080–6400	5760	240	220
Northern Cocos and Pacific	4860–6610	5710	300	330
Pacific	4860–6610	5660	190	290
Cocos	4940–6600	5800	290	260
Cocos and Pacific	4860–6610	5740	260	270

magma sills is shown in Figures 1 and 9–11. The AML reflection persists throughout the entire section with variable width (Figures 9–11) [*Carton et al*., 2010]. The width of the AML reflector is ~1 km from 9°42′N to 9°50′N, it decreases to ~500–700 m at 9°50′N, and it is widest (~2 km) at 9°51′N. From 9°51′N to 9°57′N, the AML width is ~1 km.

The upper-crust magma lenses to the east of the ridge axis from 9°52.5′N to 9°56′N are located 0.7–0.8 s TWTT below seafloor (bsf) with the shallower ones closer to the ridge axis. A deeper OAML is present at ~7.5 km east of the ridge axis in the lower crust at ~1.35 s TWTT bsf. These OAMLs were previously reported by *Canales et al*. [2012]. The lenses to the west of the ridge axis from 9°51′N to 9°52′N are lower crustal magma lenses and are located ~5 and ~3.5 km from the rise axis at 1.22 and 1.75 s bsf, respectively. Two lower-crust magma lenses are also found at 9°48′N. These lenses are located ~1.5 km from the ridge axis at 1.8 s bsf, are ~1.2 km apart, and are ~120 ms above Moho. The lower-crust magma lens at 9°41′N that appears at 1.64 s bsf is ~10 km from the ridge axis, and the small upper-crust magma lens at 9°41′N is about 1 s bsf and ~16 km from the ridge axis.

5. Discussion

We focus the discussion of our results on three primary topics: crustal thickness variation, ridge segmentation, and style of crustal accretion.

5.1. Crustal Thickness

Average crustal thickness in the study area (5740 m), on each plate (Pacific 5660 m, Cocos 5800 m), and for each of the four subareas varies only within the estimated errors (Figure 8b and Table 2), suggesting an overall uniform crustal production for the last 180 Ka. Furthermore, the small estimated differences in

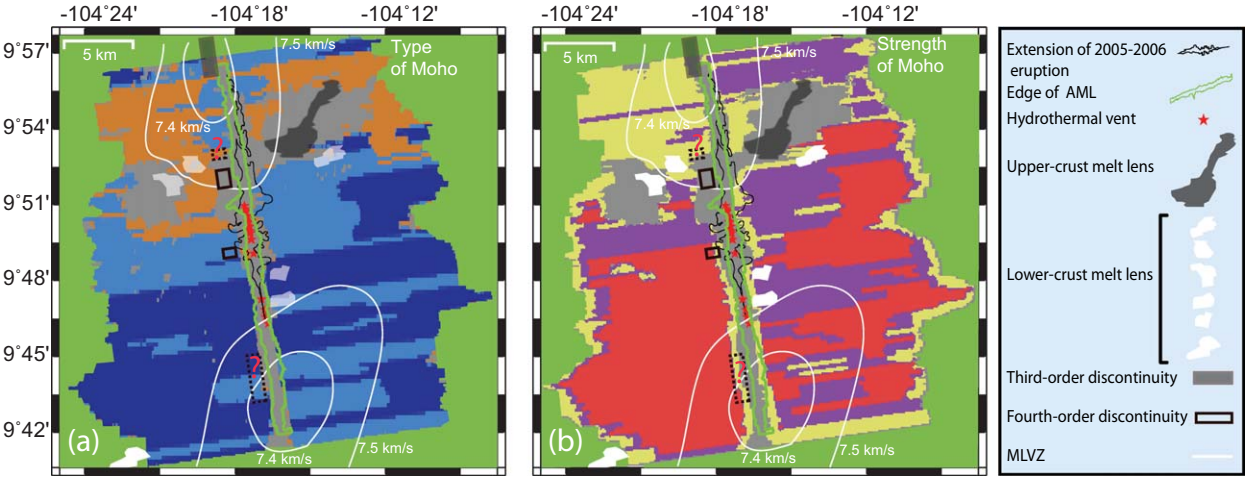

Figure 9. MTZ reflection (a) character and (b) reflection strength from this work, and their spatial relationship with magmatic segmentation, hydrothermal activity, and mantle low-velocity zones (MLVZs). Black dotted rectangles with red question marks are locations of disputed discontinuities. Location of MLVZ contours is from *Toomey et al*. [2007]. Edge of the AMC is from *Carton et al*. [2010]. Color scale is the same as for Figure 6. Source of other information same as in Figure 1.

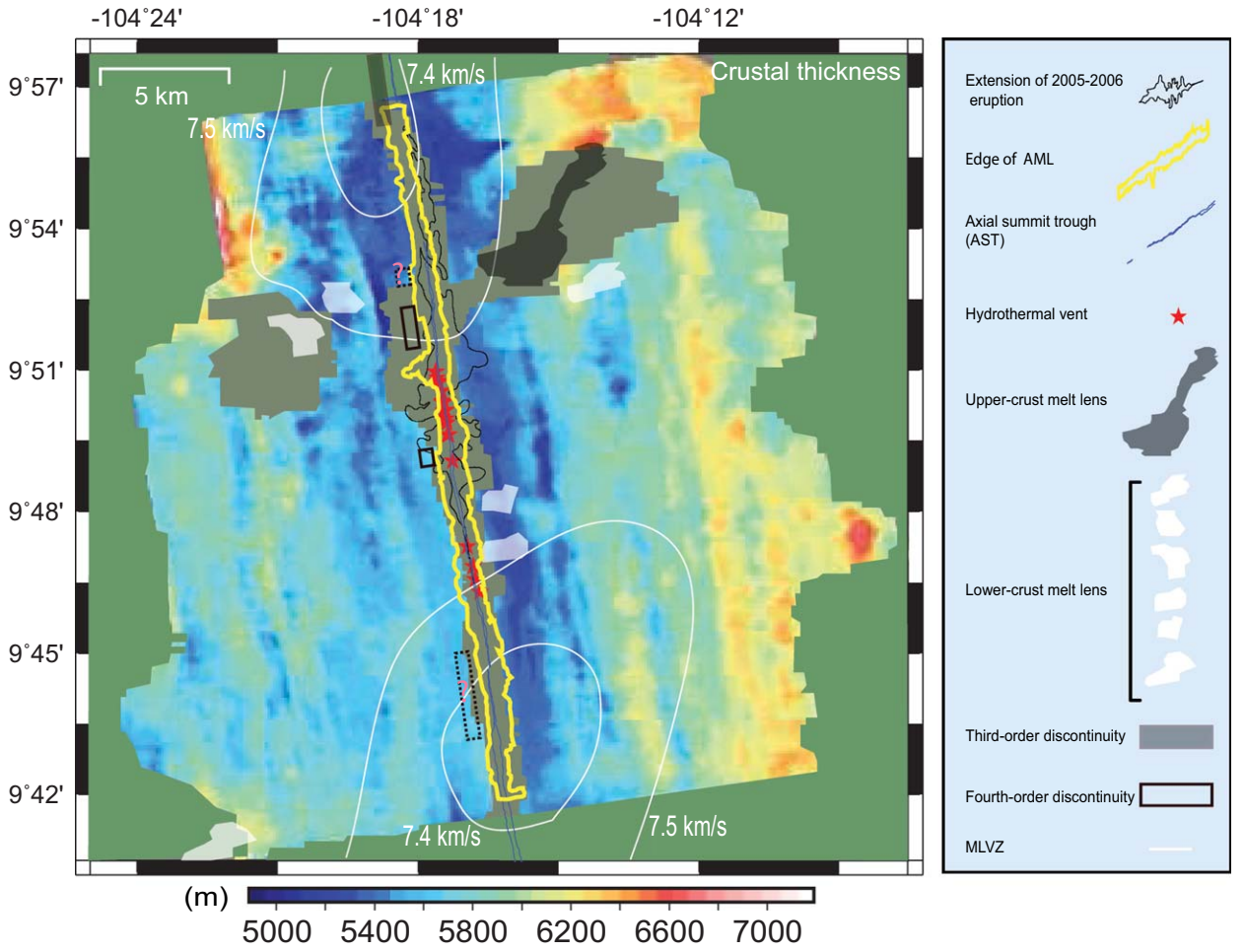

Figure 10. Crustal thickness from Figure 7d is shown together with the location of magmatic segmentation, hydrothermal activity, MLVZs, OAMLs, AML, AST, and extent of 2005–2006 volcanic eruption. Black dotted rectangles with red question marks are locations of disputed discontinuities. Source of information is same as in Figures 1 and 9.

crustal thickness between the two plates could arise from errors in the velocity models used for depth conversion. The average *P*-wave velocities used here for depth conversion are ~3% lower on the Pacific plate than the *P*-wave velocities on the Cocos plate. If the velocities on both ridge flanks were the same, then the measured average crustal thickness on the Pacific and Cocos plates would differ by only 30 m or 0.5%. Uncertainties in the velocity models used for depth conversion are large (325 m/s) due to the sparseness of the 2-D OBS profiles used to form the 3-D interval velocity model for depth conversion, and are about twice that of the difference in the average velocity between the two flanks.

Individual thickness measurements, however, can differ significantly beyond the error bounds, with the thinnest (4860 m) and thickest (6610 m) crust measured giving a crustal thickness range of 1.75 km. This value falls within the range of crustal thickness variation (1.3–1.8 km) for the second-order EPR segment between 9°15′N and 9°50′N derived from the wide-angle OBS study of *Canales et al*. [2003], and it is about 70% of the crustal thickness variation (~2.3 km) in the same latitude range derived from the MCS study of *Barth and Mutter* [1996]. For the latitude range coincident with our 3-D survey, the crustal thickness derived from the wide-angle OBS study of *Canales et al*. [2003] shows variation of ~1 km. The MCS study of *Barth and Mutter* [1996] is coincident with only the southern half of our 3-D survey area (9°42′N–9°50′N). Within this area, their MCS-derived crustal thickness shows a variation of ~1.5 km. However, the *Canales et al*. [2003] and *Barth and Mutter* [1996] studies cover a much larger surface area even within the latitude range coincident with our 3-D survey because they extend to older crust. Therefore, the results of this study indicate that the variation in thickness of normal oceanic crust formed at fast-spreading centers is, perhaps,

Table 3. Computed Crustal Thickness Range and Mean After Removing Layer 2A With Associated Standard Deviation and Average Propagated Error for the Investigated Section of the EPR, Pacific and Cocos Plates, and Various Parts of the Study Area

Plate Section	Range (m)	Mean Value (m)	Standard Deviation (m)	Average Propagation Error (m)
Southern Cocos	4910–5975	5450	220	230
Northern Cocos	4690–6380	5450	300	310
Southern Pacific	5110–5790	5420	100	230
Northern Pacific	4660–6093	5300	200	380
Southern Cocos and Pacific	4910–5975	5430	170	230
Northern Cocos and Pacific	4660–6380	5370	270	340
Pacific	4660–6093	5370	160	300
Cocos	4690–6380	5450	250	270
Cocos and Pacific	4660–6380	5410	220	280

even greater than that observed with earlier studies of *Barth and Mutter* [1996] and *Canales et al*. [2003], and can occur over areas comparable in size to small-scale ridge segmentation.

Taken together, the *Barth and Mutter* [1996], *Canales et al*. [2003], and this study all consistently show that the crust produced at the fast-spreading EPR varies less in thickness than the crust found along an individual segment of a slow spreading center where this variation is ~4 km [e.g., *Tolstoy et al*., 1993]. Nevertheless, the crustal thickness variation observed at the EPR is significant considering that some modeling studies [e.g., *Lin and Phipps Morgan*, 1992] predict the mantle upwelling and melt delivery at fast-spreading centers to be more 2-D or sheet-like beneath the ridge axis and therefore that the crustal thickness is expected to be mostly uniform. This contrasts with the slow spreading centers where the mantle upwelling and melt delivery is thought to be more 3-D with large variations in crustal thickness predicted [e.g., *Forsyth*, 1992].

The average crustal thickness of 5740 ± 270 m from the results of detailed 3-D MCS reflection imaging carried out in this work is about 5% greater than the average crustal thickness of ~5500 m estimated for our study area by *Barth and Mutter* [1996] and based on 2-D MCS profiles spaced some 3 km apart. Despite the difference in thickness, the two results agree within the error limits. The average crustal thickness of ~6.8 km for the same area and based on the wide-angle OBS results of *Canales et al*. [2003] is significantly larger than obtained from the reflection data. This is not surprising because reflection and refraction estimates of crustal thickness are likely to differ if the transition from lower crustal to mantle velocities is through a thick MTZ, as opposed to a single step in velocity. Indeed, crustal thickness estimates based on reflection imaging are calculated down to the top of the MTZ based on the onset in TWTT of the Moho reflection, whereas refraction studies constrain the entire gradient region associated with the MTZ and thus can provide thickness values down to the base of this gradient zone. The advantage of using both methods is that they provide complementary information about the subsurface and in this particular case tell us that the average thickness of the MTZ in the study area is about 1 km. Earlier estimates of the MTZ thickness from ESP data on-axis and 10 km off-axis axis at ~9°35′N are 0.5 and 1.7 km, respectively [*Vera et al*., 1990]. Our 1 km average MTZ thickness is consistent with these earlier results. We could not compute crustal thickness for the areas where the AML and the main grouping of OAMLs occur because the Moho reflection was not imaged there (Figures 9–11). Three likely reasons for not imaging Moho reflections in these areas are: (a) Moho is not yet formed below the AML at zero or near zero crustal age; (b) Moho is overprinted by the ascending melt at major OAML locations; and (c) standard reflection imaging methodology used in this study is not adequate for imaging the Moho beneath the AML and OAMLs, which are characterized by large lateral velocity variations and high seismic attenuation [e.g., *Dunn et al*., 2000; *Wilcock et al*., 1995; *Canales et al*., 2012].

Excluding the area in the vicinity of the Lamont seamount on the Pacific plate, which for most part is not taken into account for crustal thickness computations in this work because of its anomalous nature, the thickest crust in the study area is found at ~9°56′N on the Cocos plate, some 5 km east from the ridge axis in a region bounded by the large east flank OAMLs to the south and the Watch Stander seamounts to the north [*Scheirer and Macdonald*, 1995]. This locally thick crust could reflect significant crustal underplating associated with seamount magmatism.

To investigate the effect of layer 2A on crustal thickness variations within our study area, we calculated its thickness and removed it from the total crustal thickness (Figure 11). Statistical analysis for the combined layer 2B and 3 thickness is summarized in Table 3. The propagated error is updated to incorporate an 80 m uncertainty for layer 2A thickness inferred from an earlier study on the Juan de Fuca Ridge [*Nedimović et al*.,

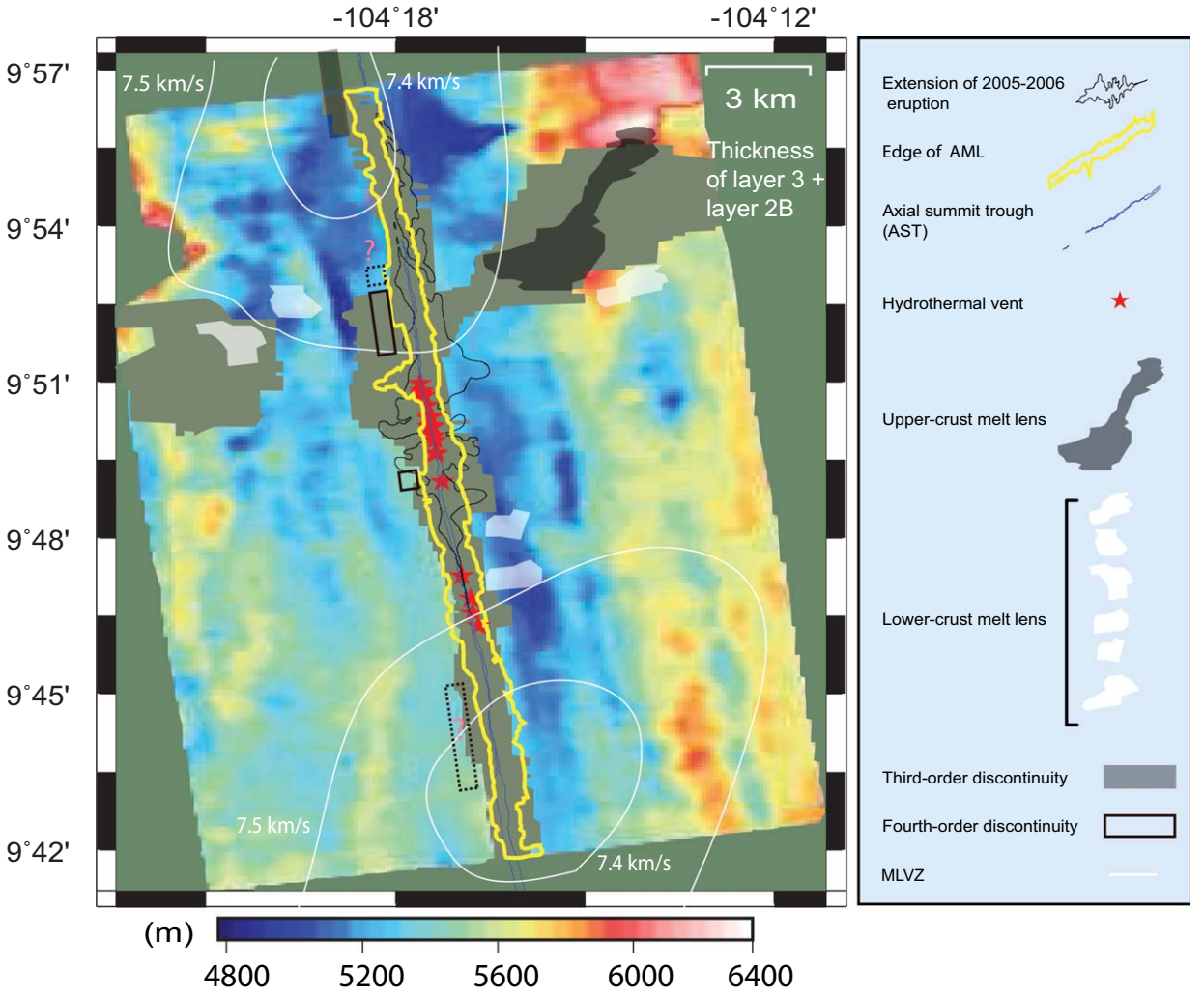

Figure 11. Crustal thickness from Figure 7d after removing layer 2A is shown together with the location of magmatic segmentation, hydrothermal activity, MLVZs, OAMLs, AML, AST, and extent of 2005–2006 volcanic eruption. Black dotted rectangles with red question marks are locations of disputed discontinuities. Source of information is same as in Figures 1 and 9.

2008]. The results show that in our study area the variations in the layer 2A thickness have only a minor impact on the variations in the total crustal thickness and do not impact the conclusions reached.

5.2. Ridge Segmentation

Existing models of ridge segmentation for our study area (e.g., Figures 11 and 12a) are based on seafloor structures, geochemical investigations, tomographic inversions, and the results from MCS reflection imaging of the AML [e.g., *Langmuir et al.*, 1986; *Macdonald et al.*, 1988, 1992; *Haymon et al.*, 1991, *Haymon and White*, 2004; *Kent et al.*, 1993; *Dunn et al.*, 2000; *White et al.*, 2002, 2006; *Toomey et al.*, 2007; *Carbotte et al.*, 2013]. Information on the MTZ character and crustal thickness derived in this work provides a complementary, mantle melt delivery related view into the ridge segmentation. The thickness of the oceanic crust is a measure of the volume of melt extracted from the underlying mantle and has been used to study magmatic segmentation along MORs [e.g., *Forsyth*, 1992]. The thickness of the MTZ is a measure of the volume of gabbro melt at the crust-mantle boundary [e.g., *Nicolas et al.*, 1996], thus also providing information on the distribution and delivery of mantle melt along the ridge axis.

We hypothesize that if segmentation arises from processes of melt distribution and delivery in the upper mantle, then MTZ character and/or crustal thickness may vary from one segment to another. To evaluate our hypothesis, we first compute average crustal thickness for the near axial region (Figure 12a). The

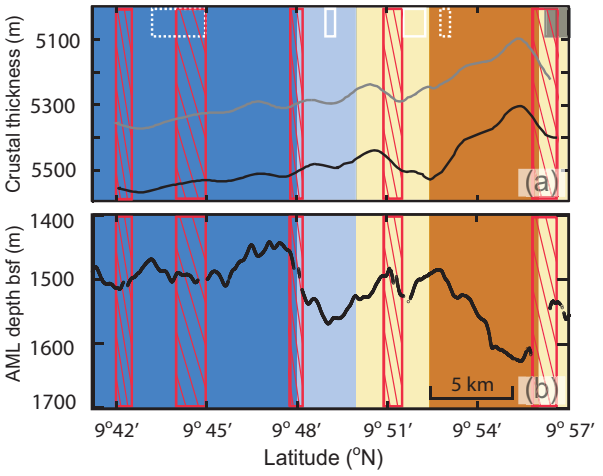

Figure 12. Relationship between the MTZ character (background; see Figure 6 for color code) and: (a) MCS-derived crustal thickness with (black line) and without (gray line) layer 2A, (b) AML depth bsf. The MCS crustal thickness in Figure 12a is average crustal thickness for the area near the ridge axis (±0.5–3.0 km or crust ~10–55 Ka old). The AML depth bsf is from *Carbotte et al.* [2013]. The background color indicates the dominant MTZ type on both flanks as a function of latitude. Transitional areas, where no particular MTZ type dominates, are shown in yellow. White rectangles are fourth-order and filled gray rectangles are third-order segment discontinuities [*White et al.*, 2002, 2006; *Haymon and White*, 2004; *Carbotte et al.*, 2013]. Dotted white rectangles show the location of disputed small-scale segment discontinuities. Red rectangles are AML disruption zones from *Carbotte et al.* [2013].

average crustal thickness was computed on crust from 0.5 to 3.0 km away from the ridge axis (crust ~10–55 Ka old) to characterize the effects of present and recent segmentation processes on crustal thickness [e.g., *Dunn et al.*, 2000]. To remove the potential bias from variations in layer 2A thickness, which varies along the axis in the study area [*Tian et al.*, 2000; *Sohn et al.*, 2004], the crustal thickness is shown with and without layer 2A (Figure 12a). We then compare crustal thickness and MTZ characteristics with the third-order and fourth-order segmentation previously identified in this region based on seafloor indicators (Figures 9 and 12a) [e.g., *White et al.*, 2002, 2006; *Haymon et al.*, 1991; *Carbotte et al.*, 2013]. By using the inferred crustal thickness and MTZ character signatures of the undisputed third-order and fourth-order segment discontinuities from these studies, we re-evaluate the disputed discontinuities and evaluate other changes in crustal thickness and MTZ character along the ridge axis.

The undisputed third-order discontinuity identified within our study area based on the seafloor morphology, geochemical investigations, and reflection imaging of the AML [e.g., *Langmuir et al.*, 1986; *Macdonald et al.*, 1988, 1992; *Haymon et al.*, 1991, *Haymon and White*, 2004; *White et al.*, 2002, 2006; *Carbotte et al.*, 2013] is centered at 9°56′N–9°58′N. Only the interpretation of mantle tomography results [*Toomey et al.*, 2007], which places the center of third-order segments at the location of mantle low-velocity zone (MLVZ) bulls eyes and is regionally (8°30′N–9°50′N) consistent with the interpretation of segmentation based on the other methods [*Toomey et al.*, 2007], disagrees with this location of a third-order segment boundary. The MLVZ bulls eye found at ~9°56′N is located close to the northern edge of the OBS survey and it is possible that it is characterized by greater uncertainty in its geographic location due to the sparser ray coverage in this area [*Toomey et al.*, 2007].

The 9°56′N–9°58′N third-order discontinuity appears to be associated with a change in both the MTZ character and crustal thickness (Figure 12a). Both the MTZ and crust are inferred to thin from ~9°56′N to 9°57′N, where our 3-D reflection cube ends, supporting earlier interpretations of a third-order boundary in this area between segments that behave as independent magmatic units each with a unique mantle melt source. The undisputed fourth-order discontinuity at 9°49′N is found in an area mostly characterized by a thin MTZ (shingled reflection Moho, Figure 12a). The lack of variation in the Moho reflection combined with little change in crustal thickness observed in this area indicates that this discontinuity does not correspond with a crustal scale transition. These observations of MTZ character and crustal thickness are consistent with the hypothesis that third-order segment-scale variations in magma supply are related to mantle melt extraction processes occurring near the Moho, whereas smaller-scale fourth-order segmentation arises from the processes related to the crustal magma system [*Macdonald et al.*, 1988; *Langmuir et al.*, 1986; *Toomey and Hooft*, 2008].

The debated third-order or fourth-order discontinuity at ~9°45′N (Figure 12a) [*White et al.*, 2002] is located in an area also void of variations in MTZ character and crustal thickness and we favor interpretation of this feature as a fourth-order discontinuity. The fourth-order discontinuity variably located at 9°51.5′N [*White et al.*, 2002] or 9°53′N [*White et al.*, 2006] falls within a zone of change in both the MTZ character and crustal thickness (Figure 12a) that is similar to that found at the third-order ridge discontinuity at 9°50′N–9°52.5′N.

This evidence of a crustal transition suggests a change in the magmatic system in the shallowest mantle coincident with this location and, on this basis, we favor a third-order classification for this offset.

5.3. Crustal Accretion Style

Lower crustal accretion models from multiple magma bodies [e.g., *Schouten and Denham*, 1995; *Kelemen et al*., 1997; *Maclennan et al*., 2004] imply a larger volume of gabbro melt embedded in the transition from the mantle to the crust than the gabbro-glacier model and thus are characterized by a thicker MTZ [e.g., *Rabinowicz et al*., 1984; *Nicolas and Boudier*, 1995; *Kelemen and Aharonov*, 1998]. Because seismic modeling of ophiolites [e.g., *Collins et al*., 1986; *Brocher et al*., 1985] shows that thin and thick MTZs have a distinctly different reflection signature, single-phase and multiphase response, respectively, seismic reflection images that capture the MTZ character have the potential to be used to infer the lower crustal accretion style of the oceanic crust. This seems true for crust both on-axis and off-axis because a portion of the gabbro melt embedded in thick MTZs cools and solidifies in situ leaving evidence about the deep melt distribution at the time the crust was formed [e.g., *Nedimović et al*., 2005]. Using these studies as a framework, we interpret the primary results from our extensive 3-D reflection imaging, maps of the MTZ character and crustal thickness (Figures 6, 7, and 9–12a), in terms of the accretion style within the study area.

The overall character of the MTZ on both plates (Figure 12, color shading) is impulsive from ~9°42′N to 9°48′N indicating a sharp transition from the crust to mantle. The MTZ becomes mostly shingled from 9°48′N to 9°50′N, where it changes into transitional from 9°50′N to 9°52.4′N. A diffuse Moho reflection response and hence a thick MTZ is preponderant from 9°52.4′N to 9°56′N, after which it becomes transitional until the northern edge of the survey at 9°57′N. In parallel with these changes in MTZ character, the average crustal thickness for the youngest crust (calculated for crust ~10–55 Ka old; Figure 12a) gradually decreases from 9°42′N to ~9°51.5′N and more rapidly from 9°51.5′N to 9°56′N reaching a minimum at ~9°55.5′N. This spatial variability over short length scales is consistent with studies of the Bay of Island and Oman ophiolite complexes that document high degrees of lateral variation in the internal structure of the crust and MTZ in these paleo-ridge environments [*Karson et al*., 1984; *Brocher et al*., 1985; *Benn et al*., 1988; *Nicolas and Boudier*, 1995].

From the spatial variations in MTZ character, we infer that the style of crustal accretion varies in the study area with more efficient extraction of mantle melts to the crust in the southern part of our survey (9°42′N–9°49.5′N) and perhaps more of the crust formed from the AML. Measured crustal thickness variation is small, at the limit of what we can resolve, suggesting that the mantle melt supply does not vary significantly for our study area. The northern half of the survey area (9°49.5′N–9°57′N) is also associated with greater off-axis magmatism as inferred from the imaged OAML distribution (e.g., Figure 10) and deeper AML (Figure 12b), which may be related to less focused upper mantle magma delivery to the axis and therefore its broader distribution within the MTZ.

From a study of major element and volatile concentrations in olivine-hosted melt inclusions from lavas sampled at 9°50′N, *Wanless and Shaw* [2012] infer that magma crystallization occurs over a wide range of depths. Over 50% of crystallization appears to occur at depths consistent with crystallization within the AML whereas >25% of crystallization takes place in the lower crust or mantle. These results contrast with samples from 12°48′N where *Wanless and Shaw* [2012] infer that practically all crystallization occurred at shallow depths in the crust. The nature of the MTZ in these two areas differs. In the 9°50′N region, where significant crystallization at lower crustal/upper mantle depths is inferred, the MTZ is transitional, thin on the Cocos plate and thick on the Pacific plate. In contrast, an impulsive Moho reflection event is observed in 2-D seismic reflection data available from 12°48′N [*Barth and Mutter*, 1996]. These observations are consistent with the inference that the thicker/diffuse MTZ is associated with more of a multiple magma sill mode of accretion. While these results are suggestive, clearly the data are sparse and further melt-inclusion studies would be needed to evaluate the linkages between MTZ character and crystallization depths, for example within the thin MTZ (e.g., 9°45′N) and a thick MTZ (e.g., 9°54′N) regions in our study area.

Compliance measurements within or near our study area have been made at 9°48′N, 9°47′N, and 9°41′N (Figure 1) [*Crawford and Webb*, 2002]. Melt in the lower crust and/or MTZ was inferred only for the on-axis area at 9°48′N. While directly beneath this region, the seismic imaging indicates a thin MTZ in the near-axis crust, this measurement is close to the transition to a thick MTZ at 9°50′N. The off-axis compliance measurement at 9°47′N showing no lower crustal/MTZ melt was taken in the area where we identify what appears

to be a small OAML in the lower crust. However, the identified OAML is very small and characterized by weak signal-to-noise ratio suggesting small amounts of melt that may be below the sensitivity threshold of the compliance method. Future compliance measurements at 9°45′N and 9°54′N would be particularly useful for further correlation tests with the seismic reflection imaging results.

Thermodynamic modeling of melt migration across a section of the northern EPR that includes our study area [*Durant et al*., 2009; *Durant*, 2011] suggests that axis-centered mantle melt delivery is associated with a gabbro-glacier mode of crustal accretion, where the majority of the lower crust is formed from subsiding cumulates originating from the AML [e.g., *Henstock et al*., 1993; *Phipps Morgan and Chen*, 1993], while off-axis mantle melt delivery is associated with multiple magma body modes of lower-crustal accretion [e.g., *Maclennan et al*., 2004]. There are two bulls-eye shaped mantle low-velocity zones (MLVZs), generally interpreted to indicate higher melt concentrations, within our study area (e.g., Figures 10 and 11) [*Toomey et al*., 2007]. The approximate extent of these two bulls eyes is from 9°42′N to 9°47′N and from 9°52′N to 9°57′N. While the northern MLVZ shows a slightly greater degree of skewness with its center shifted somewhat toward the Pacific plate, both MLVZs are mostly centered beneath the ridge axis suggesting similar axis-centered mantle melt delivery and therefore mode of crustal accretion at both locations. However, we infer a major difference in the MTZ thickness between the two MLVZs and that the style of crustal accretion likely differs between the two locations. The location of the northern MLVZ corresponds with our zone of inferred thick MTZ and thinner crust, while the southern MLVZ corresponds with the thin MTZ and thicker crust. Interestingly, the region between the two MLVZ corresponds with our transitional MTZ (e.g., Figures 11 and 12).

Within our study area, south-to-north variations in mantle melt delivery and crustal accretion style are interpreted from regional changes in the character of the MTZ and possible minor changes in crustal thickness. We speculate that these variations reflect more diffuse melt delivery to the ridge axis in the north due to the influence of small off-axis melt anomalies associated with the prominent near-axis seamounts found in this region. The most recently formed Lamont seamount is located at the very NW corner of our 3-D box, and the Watch Stander seamounts on the Cocos plate are found just to the north of our survey. The concentration of the OAMLs around 9°53′N where the trend of the youngest Lamont seamounts projects to the EPR, slight skewness of the northern MLVZ toward the Pacific plate, deeper AML, as well as the thick MTZ and thinner crust in this area suggest that the local mantle melt delivery to the crust becomes increasingly defocused from south to north. This more diffuse mantle melt delivery in the north may reflect interaction between melt sources in the shallow mantle for the ridge axis and the nearby seamounts.

6. Conclusions

Analysis of the high-resolution 3-D MCS data set collected over the EPR between 9°42′N and 9°57′N has yielded a 3-D reflection cube that gives new insights into the crustal thickness, ridge segmentation, and style of crustal accretion across an area covering ~658 km^2. The MTZ reflections were imaged, and therefore crustal thickness determined, within ~87% of the study area, with 41% of the total area characterized with impulsive, 29% with shingled, and 17% with diffusive MTZ reflections. The computed average crustal thickness of 5740 ± 270 m is about 5% greater than the average crustal thickness of ~5.5 km estimated for the study area by an earlier MCS study [*Barth and Mutter*, 1996]. The average crustal thickness computed in this work varies little from Pacific to Cocos plate, as well as between the investigated study area quadrants suggesting regionally uniform crustal production in the last 180 Ka. However, individual crustal thickness measurements can vary by as much as 1.75 km. This shows that the variation in thickness of normal oceanic crust formed at a fast-spreading center and covering an area comparable in size to small-scale ridge segments is significant, which suggests that mantle melt delivery at fast-spreading centers can vary over short spatial scales.

Key observations pertaining to ridge segmentation that emerge from the analysis of the MTZ character and near-axis crustal thickness are: (a) The third-order ridge discontinuity at 9°56–58′N evident in the seafloor morphology of the axial zone, geochemical investigations, and MCS reflection imaging of the AML appears to be associated with a change in the MTZ character and crustal thickness; (b) These changes occur over an area 3–4 km long indicating that third-order discontinuities are not point locations, in agreement with the seafloor expression of these offsets; and (c) Fourth-order ridge discontinuities appear to show no correlation

with variations in the MTZ character and/or crustal thickness. In general, this suggests that the third-order segmentation is governed by melt distribution within the uppermost mantle while the fourth-order ridge segmentation arises from midcrustal to upper-crustal processes. In this light, we interpret the debated third-order or fourth-order ridge segment boundary at ~9°45′N as a fourth-order offset. The ridge segment boundary variably located at 9°51.5′N or 9°53′N marks a significant transition in Moho structure and, on this basis, is assigned a third-order discontinuity status centered at 9°51–51.5′N.

We infer variations in the accretion style within our study area (a) based on the main results from our extensive 3-D reflection imaging, maps of the MTZ character and crustal thickness and (b) in the context of the existing knowledge from ophiolite, geochemical, and other controlled source seismic studies. The MTZ character maps show a thin MTZ within the southern half of our survey area (9°42′N–9°49.5′N) indicating efficient mantle melt extraction to the crust and, perhaps, a greater proportion of the lower crust accreted from the AML than for the northern half (9°49.5′N–9°57′N). In the northern half of our survey area, where a thick and transitional MTZ are imaged and mantle melt delivery to the axis seems less focused, the multiple magma body mode of crustal accretion may predominate. The crustal thickness of the near-axial region is only slightly (~100 m) smaller across the northern half of the survey area. This indicates that there is little variation in the mantle melt supply within the study area and supports the inferred less efficient melt delivery for the northern area as some of the melt stays trapped in the MTZ. It remains unclear as to what is the cause for the apparent south-to-north variation in the style but not volume of the mantle to crust melt delivery and the inferred corresponding change in the crustal accretion style. However, the most likely culprit is the melt source interaction between the ridge and the Lamont seamounts.

Acknowledgments

This research was supported by the National Science Foundation grants OCE0327872 to J. C. M., S. M. C., OCE327885 to J. P. C., OCE0624401 to M. R. N., and NSERC Discovery, CRC and CFI grants to M. R. N. We are grateful to Keith Louden, Matthew Salisbury, Ginger Barth, and Doug Toomey for their comments that improved the paper.

References

Barth, G. A., and J. C. Mutter (1996), Variability in oceanic crustal thickness and structure: Multichannel seismic reflection results from the northern East Pacific Rise, *J. Geophys. Res.*, *101*, 17,951–17,975, doi:10.1029/96JB00814.

Batiza, R., and Y. Niu (1992), Petrology and magma chamber processes at the East Pacific Rise −9°30′N, *J. Geophys. Res.*, *97*, 6779–6797.

Benn, K., A. Nicolas, and I. Reuber (1988), Mantle-crust transition zone and origin of wehrlitic magmas: Evidence from the Oman ophiolite, *Tectonophysics*, *151*, 75–85.

Boudier, F., A. Nicolas, and B. Ildefonse (1996), Magma chambers in the Oman ophiolite: Fed from the top and the bottom, *Earth Planet. Sci. Lett.*, *144*, 239–250.

Brocher, T. A., J. A. Karson, and J. A. Collins (1985), Seismic stratigraphy of the oceanic Moho based on ophiolite models, *Geology*, *13*, 62–65.

Canales, J. P., R. S. Detrick, D. R. Toomey, and W. S. D. Wilcock (2003), Segment scale variations in the crustal structure of 150–300 kyr old fast-spreading oceanic crust (East Pacific Rise, 8°15′N–10°5′N) from wide-angle seismic refraction profiles, *Geophys. J. Int.*, *152*(3), 766–794, doi:10.1046/j.1365-246X.2003.01885.x.

Canales, J. P., M. R. Nedimović, G. M. Kent, S. M. Carbotte, and R. S. Detrick (2009), Seismic reflection images of a near-axis melt sill within the lower crust at the Juan de Fuca ridge, *Nature*, *460*, 89–93, doi:10.1038/nature08095.

Canales, J. P., H. Carton, S. M. Carbotte, J. C. Mutter, M. R. Nedimović, M. Xu, O. Aghaei, M. Marjanović, and K. Newman (2012), Network of off-axis melt bodies at the East Pacific Rise. *Nat. Geosci.*, *5*, 279–283, doi:10.1038/NGEO1377.

Carbotte, S., and K. Macdonald (1992), East Pacific Rise 8°–10°30′N: Evolution of ridge segments and discontinuities from SeaMARC II and three-dimensional magnetic studies, *J. Geophys. Res.*, *97*, 6959–6982, doi:10.1029/91JB03065.

Carbotte, S., G. Ponce-Correa, and A. Solomon (2000), Evaluation of morphological indicators of magma supply and segmentation from a seismic reflection study of the EPR 15°30–17°N, *J. Geophys. Res.*, *105*, 2737–2759.

Carbotte, S. M., M. Marjanović, H. Carton, J. C. Mutter, J. P. Canales, M. R. Nedimović, S. Han, and M. R. Perfit (2013), Fine-scale segmentation of the crustal magma reservoir beneath the East Pacific Rise, *Nat. Geosci.*, *6*, 866–870, doi:10.1038/ngeo1933.

Carton, H. D., S. M. Carbotte, J. C. Mutter, J. P. Canales, M. R. Nedimović, O. Aghaei, M. Marjanović, and K. R. Newman (2010), Three-dimensional seismic reflection images of axial melt lens and seismic layer 2A between 9°42′N and 9°57′N on the East Pacific Rise, Abstract OS21C-1514 presented at 2010 Fall Meeting, 13–17 December, AGU, San Francisco, Calif.

Chen, Y. J., and J. Phipps Morgan (1996), The effects of spreading rate, the magma budget, and the geometry of magma emplacement on the axial heat flux at mid-ocean ridges, *J. Geophys. Res.*, *101*, 11,475–11,482.

Choo, J., J. Downton, and J. Dewar (2004), Lift: A new and practical approach to noise and multiple attenuation, *First Break*, *22*, 39–44.

Christeson, G. L., G. M. Purdy, and G. J. Fryer (1992), Structure of young upper crust at the East Pacific Rise near 9°30′N, *Geophys. Res. Lett.*, *19*, 1045–1048.

Collins, J. A., T. M. Brocher, and J. A. Karson (1986), Two-dimensional seismic reflection modeling of the inferred crust-mantle transition in the Bay of Islands Ophiolite, *J. Geophys. Res.*, *91*, 12,520–12,538.

Crawford, W. C., and S. C. Webb (2002), Variations in the distribution of magma in the lower crust and at the Moho beneath the East Pacific Rise at 9°–10°N, *Earth Planet. Sci. Lett.*, *203*, 117–130, doi:10.1016/S0012–821X(02)00831-2.

Detrick, R. S., P. Buhl, E. Vera, J. Mutter, J. Orcutt, J. Madsen, and T. Brocher (1987), Multi-channel seismic imaging of a crustal magma chamber along the East Pacific Rise, *Nature*, *326*, 35–41.

Dunn, R. A., D. R. Toomey, and S. C. Solomon (2000), Three-dimensional seismic structure and physical properties of the crust and shallow mantle beneath the East Pacific Rise at 9°30′N, *J. Geophys. Res.*, *105*, 23,537–23,555, doi:10.1029/2000JB900210.

Durant, D. T. (2011), *Effects of the off-axis melt supply at fast-spreading mid-ocean ridges: A study of the 9°–10°N region of the East Pacific Rise*, PhD thesis, Dep. of Geol. Sci., Univ. of Oreg., Eugene, Oreg.

Durant, D. T., D. R. Toomey, and P. J. Wallace (2009), On the contribution of crystal fractionation to axial depth along the East Pacific Rise, *Eos Trans. AGU*, *90*(52), Fall Meet. Suppl., Abstract OS13A-1188.

Forsyth, D. W. (1992), Geophysical constraints on mantle flow and melt migration beneath mid-ocean ridges, in Mantle Flow and Melt Generation at Mid-ocean Ridges, Geophys. Monogr. Ser., vol. *71*, edited by J. Phipps Morgan et al., pp. 1–65, AGU, Washington, D. C.

Han, S., H. D. Carton, S. M. Carbotte, J. C. Mutter, J. Canales, and M. R. Nedimović (2011), 3D seismic reflection images of an off-axis melt lens and its associated upper crust around 9°39′N, East Pacific Rise, Abstract OS22A-02 presented at 2011 Fall Meeting, AGU, San Francisco, Calif., 5–9 Dec.

Harding, A. J., G. M. Kent, and J. A. Orcutt (1993), A multichannel seismic investigation of upper crustal structure at 9°N on the East Pacific Rise: Implications for crustal accretion, *J. Geophys. Res.*, *98*, 13,925–13,944.

Haymon, R. M., and S. M. White (2004), Fine-scale segmentation of volcanic/hydrothermal systems along fast-spreading ridge crests, *Earth Planet. Sci. Lett.*, *226*, 367–382, doi:10.1016/j.epsl.2004.08.002.

Haymon, R. M., D. J. Fornari, M. H. Edwards, S. M. Carbotte, D. Wright, and K. C. Macdonald (1991), Hydrothermal vent distribution along the East Pacific Rise crest (9°9′–54′N) and its relationship to magmatic and tectonic processes on fast spreading mid-ocean ridges, *Earth Planet. Sci. Lett.*, *104*, 513–534, doi:10.1016/0012–821X(91)90226-8.

Haymon, R. M., et al. (1993), Volcanic eruption of the mid-ocean ridge along the East Pacific Rise crest at 9°45′–52′N: Direct submersible observations of seafloor phenomena associated with an eruption event in April, 1991, *Earth Planet. Sci. Lett.*, *119*, 85–101, doi:10.1016/0012–821X(93)90008-W.

Henstock, T. J., A. W. Woods, and R. S. White (1993), The accretion of oceanic crust by episodic sill intrusion, *J. Geophys. Res.*, *98*, 4143–4161.

Herron, T. J., P. L. Stoffa, and P. Buhl (1980), Magma chamber and mantle reflections—East Pacific Rise, *Geophys. Res. Lett.*, *7*, 989–992.

Karson, J. A., J. A. Collins, and J. F. Casey (1984), Geologic and seismic velocity structure of the crust/mantle transition in the Bay of Islands ophiolite complex, *J. Geophys. Res.*, *89*, 6126–6138, doi:10.1029/JB089iB07p06126.

Kelemen, P. B., K. Koga, and N. Shimizu (1997), Geochemistry of gabbro sills in the crust-mantle transition zone of the Oman ophiolite: Implications for the origin of the oceanic lower crust, *Earth Planet. Sci. Lett.*, *146*, 475–488.

Kelemen, P. B., and E. Aharonov (1998), Periodic formation of magma fractures and generation of layered gabbros in the lower crust beneath oceanic spreading ridges, in Faulting and Magmatism at Mid-Ocean Ridges, Geophys. Monogr. Ser., vol. *106*, edited by W. R. Buck et al., pp. 267–289, AGU, Washington, D. C.

Kent, G. M., A. J. Harding, and J. A. Orcutt (1990), Evidence for a smaller magma chamber beneath the East Pacific Rise at 9°30′N, *Nature*, *344*, 650–653.

Kent, G. M., A. J. Harding, and J. A. Orcutt (1993), Distribution of magma beneath the East Pacific Rise between the Clipperton transform and the 9°17′N deval from forward modeling of common depth point data, *J. Geophys. Res.*, *98*, 13,945–13,969.

Kent, G. M., A. J. Harding, J. A. Orcutt, R. S. Detrick, J. C. Mutter, and P. Buhl (1994), Uniform accretion of oceanic crust south of the Garrett transform at 14°15′S on the East Pacific Rise, *J. Geophys. Res.*, *99*, 9097–9116, doi:10.1029/93JB02872.

Langmuir, C. H., J. F. Bender, and R. Batiza (1986), Petrological and tectonic segmentation of the East Pacific Rise, 5°30′N–14°30′N, *Nature*, *322*, 422–429.

Lin, J., and J. Phipps Morgan (1992), The spreading rate dependence of three-dimensional mid-ocean ridge gravity structure, *Geophys. Res. Lett.*, *19*, 13–16.

Macdonald, K. C. (1998), Periodic formation of magma fractures and generation of layered gabbros in the lower crust beneath oceanic spreading ridges, in Faulting and Magmatism at Mid-Ocean Ridges, Geophys. Monogr. Ser., vol. *106*, edited by W. R. Buck et al., pp. 27–58, AGU, Washington, D. C.

Macdonald, K. C., J. C. Sempere, and P. J. Fox (1984), East Pacific Rise from Siqueiros to Orozco fracture zones: Along strike continuity of axial neovolcanic zone and structure and evolution of overlapping spreading centers, *J. Geophys. Res.*, *89*, 6049–6069.

Macdonald, K. C., P. J. Fox, L. J. Perram, M. F. Eisen, R. M. Haymon, S. P. Miller, S. M. Carbotte, M.-H. Cormier, and A. N. Shor (1988), A new view of the mid-ocean ridge from the behavior of ridge axis discontinuities, *Nature*, *335*, 217–225, doi:10.1038/335217a0.

Macdonald, K. C., et al. (1992), The East Pacific Rise and its flanks 8°–18°N: History of segmentation, propagation and spreading direction based on SeaMARC II and SeaBeam studies, *Mar. Geophys. Res.*, *14*, 299–344.

Maclennan, J., T. Hulme, and S. C. Singh (2004), Thermal models of oceanic crustal accretion: Linking geophysical, geological and petrological observations, *Geochem. Geophys. Geosyst.*, *5*, Q02F25, doi:10.1029/2003GC000605.

Mutter, J. C., S. M. Carbotte, M. R. Nedimović, J. P. Canales, and H. Carton (2009), Seismic imaging in three dimensions on the East Pacific Rise, *Eos Trans. AGU*, *90*, 374–375, doi:10.1029/2009EO420002.

Nedimović, M. R., S. M. Carbotte, A. J. Harding, R. S. Detrick, J. P. Canales, J. B. Diebold, G. M. Kent, M. Tischer, and J. M. Babcock (2005), Frozen magma lenses below the oceanic crust, *Nature*, *436*, 1149–1152, doi:10.1038/nature03944.

Nedimović, M. R., S. M. Carbotte, J. B. Diebold, A. J. Harding, J. P. Canales, and G. M. Kent (2008), Upper crustal evolution along the Juan de Fuca Ridge flanks, *Geochem. Geophys. Geosyst.*, *9*, Q09006, doi:10.1029/2008GC002085.

Nicolas, A., and F. Boudier (1995), Mapping oceanic ridge segments in Oman ophiolites, *J. Geophys. Res.*, *100*, 6179–6197.

Nicolas, A., F. Boudier, and B. Ildefonse (1996), Variable crustal thickness in the Oman Ophiolite: Implication for oceanic crust, *J. Geophys. Res.*, *101*, 17,941–17,950.

Orcutt, J., N. Kennett, L. Dorman, and W. Prothero (1975), A low-velocity zone underlying a fast-spreading ridge crest, *Nature*, *256*, 475–476.

Phipps Morgan, J., and Y. Chen (1993), The genesis of oceanic crust, magma injection, hydrothermal circulation and crustal flow, *J. Geophys. Res.*, *98*, 6283–6297.

Pratt, R. G., and M. H. Worthington (1990), Inverse theory applied to multi-source cross-hole tomography. Part I: Acoustic wave-equation method, *Geophys. Prospect.*, *38*, 287–310.

Quick, J. E., and R. P. Delinger (1993), Ductile deformation and the origin of layered gabbro in ophiolites, *J. Geophys. Res.*, *98*, 14,015–14,027.

Rabinowicz, M., A. Nicolas, and J. Vigneresse (1984), A rolling mill effect in the asthenosphere beneath oceanic spreading centers, *Earth Planet. Sci. Lett.*, *67*, 97–108, doi:10.1016/0012–821X(84)90042-6.

Raitt, R. W. (1956), Seismic-refraction studies of the Pacific Ocean Basin, *Bull. Geol. Soc. Am.*, *67*, 1623–1640.

Reynolds, J. R., C. H. Langmuir, J. F. Bender, K. A. Kastens, and W. B. F. Ryan (1992), Spatial and temporal variability in the geochemistry of basalts from the East Pacific Rise, *Nature*, *359*, 493–499.

Scheirer, D. S., and K. C. Macdonald (1993), Variation in cross-sectional area of the axial ridge along the East Pacific Rise: Evidence for the magmatic budget of a fast-spreading center, *J. Geophys. Res.*, *98*, 7871–7885, doi:10.1029/93JB00015.

Scheirer, D. S., and K. C. Macdonald (1995), Near-axis seamounts on the flanks of the East Pacific Rise 8°N to 17°N, *J. Geophys. Res.*, *100*, 2239–2259.

Schouten, H., and C. Denham (1995), Virtual ocean crust, *Eos Trans. AGU*, *76*(17), Spring Meet. Suppl., S84.

Singh, S. C., et al. (2006), Seismic reflection images of the Moho underlying melt sills at the East Pacific Rise, *Nature*, *442*, 287–290.

Sinton, J. M., S. M. Smaglik, J. J. Mahoney, and K. C. Macdonald (1991), Magmatic processes at superfast spreading mid-ocean ridges: Glass compositional variations along the East Pacific Rise 13°–23°S, *J. Geophys. Res.*, *96*, 6133–6155.

Smith, M. C., M. R. Perfit, D. J. Fornari, W. I. Ridley, M. E. Edwards, G. Kurras, and K. L. Von Damm (2001), Magmatic processes and segmentation at a fast spreading mid-ocean ridge: Detailed investigation of an axial discontinuity on the East Pacific Rise crest at 9°37′N, *Geochem. Geophys. Geosyst.*, *2*, 1040, doi:10.1029/2000GC000134.

Sohn, R. A., S. C. Webb, and J. A. Hildebrand (2004), Fine-scale seismic structure of the shallow volcanic crust on the East Pacific Rise at 9°50′N, *J. Geophys. Res.*, *109*, B12104, doi:10.1029/2004JB003152.

Soule, S. A., D. J. Fornari, M. R. Perfit, and K. Rubin (2007), New insights into mid-ocean ridge volcanic processes from the 2005–2006 eruption of the East Pacific Rise, 9°46′N–9°56′N, *Geology*, *35*, 1079–1082, doi:10.1130/G23924A.1.

Soule, S. A., J. Escartín, and D. J. Fornari (2009), A record of eruption and intrusion at a fast spreading ridge axis: Axial summit trough of the East Pacific Rise 9–10°N, *Geochem. Geophys. Geosyst.*, *10*, Q10T07, doi:0.1029/2008GC002354.

Stoffa, P. L., P. Buhl, T. J. Herron, J. K. Kan, and W. J. Ludwig (1980), Mantle reflections from beneath the crestal zone of the East Pacific Rise from multi-channel seismic data, *Mar. Geol.*, *35*, 83–97.

Tian, T., S. D. Wilcock, D. R. Toomey, and R. S. Detrick (2000), Seismic heterogeneity in the upper crust near the 1991 eruption site on the East Pacific Rise, 9°50′N, *Geophys. Res. Lett.*, *27*, 2369–2372, doi:10.1029/1999GL011191.

Tolstoy, M., A. J. Harding, and J. A. Orcutt (1993), Crustal thickness on the Mid-Atlantic Ridge: Bull's-eye gravity anomalies and focused accretion, *Science*, *262*, 726–729.

Tolstoy, M., et al. (2006), A sea-floor spreading event captured by seismometers, *Science*, *314*, 1920–1922, doi:10.1126/science.1133950.

Toomey, D. R., and E. E. E. Hooft (2008), Mantle upwelling, magmatic differentiation, and the meaning of axial depth at fast-spreading ridges, *Geology*, *36*(9), 679–682.

Toomey, D. R., G. M. Purdy, S. C. Solomon, and W. S. D. Wilcock (1990), The three-dimensional seismic velocity structure of the East Pacific Rise near latitude 9°30′N, *Nature*, *347*, 639–645, doi:10.1038/347639a0.

Toomey, D. R., W. S. D. Wilcock, R. S. Detrick, and R. A. Dunn (1998), Mapping melt and matrix flow in the uppermost mantle: Preliminary results from undershooting the EPR, *EOS Trans. AGU*, *79*(45), Fall Meet. Suppl., F805.

Toomey, D. R., D. Jousselin, R. A. Dunn, W. S. D. Wilcock, and R. S. Detrick (2007), Skew of mantle upwelling beneath the East Pacific Rise governs segmentation, *Nature*, *446*, 409–414.

Toomey, D. R., R. S. Detrick, W. S. D. Wilcock (1997), Mapping melt and matrix flow in the uppermost mantle: Undershooting the East Pacific Rise between the Siqueiros and Clipperton, *R/V Maurice Ewing Leg 97–08*, Cruise Rep., p. 163, Woods Hole Oceanogr. Inst., Woods Hole, MA.

Upton, G., and I. Cook (1996), Understanding Statistics, Oxford Univ. Press, Oxford, U. K.

Vera, E. E., J. C. Mutter, P. Buhl, J. A. Orcutt, A. J. Harding, M. E. Kappus, R. S. Detrick, and T. M. Brocher (1990), The structure of 0- to 0.2-m.y.-old oceanic crust at 9°N on the East Pacific Rise from expanded spread profiles, *J. Geophys. Res.*, *95*, 15,529–15,556.

Wanless, V. D., and A. M. Shaw (2012), Lower crustal crystallization and melt evolution at mid-ocean ridges, *Nat. Geosci.*, *5*, 651–655, doi:10.1038/ngeo1552.

White, S. M., R. M. Haymon, D. J. Fornari, M. R. Perfit, and K. C. Macdonald (2002), Correlation between volcanic and tectonic segmentation of fast-spreading ridges: Evidence from volcanic structures and lava flow morphology on the East Pacific Rise at 9°–10°N, *J. Geophys. Res.*, *107*(B8), 2173, doi:10.1029/2001JB000571.

White, S. M., R. M. Haymon, and S. Carbotte (2006), A new view of ridge segmentation and near-axis volcanism at the East Pacific Rise, 8°–12°N, from EM300 multibeam bathymetry, *Geochem. Geophys. Geosyst.*, *7*, Q12O05, doi:10.1029/2006GC001407.

Wilcock, W. S. D., S. C. Solomon, G. M. Purdy, and D. R. Toomey (1995), Seismic attenuation structure of the East Pacific Rise near 9°30′N, *J. Geophys. Res.*, *100*, 24,147–24,165.